Challenge Journal of
STRUCTURAL MECHANICS

Vol.8 No.1 (2022)

Mindlin's theory buckling columns compressive strength dynamic analysis dynamic response earthquake finite element analysis finite element method mechanical properties metaheuristic algorithms modal analysis natural frequency optimization pushover analysis reinforced concrete seismic analysis seismic design seismic isolation steel silo teaching-learning based optimization [illegible]plate

TULPAR ACADEMIC PUBLISHING

ISSN 2149-8024

Challenge Journal of Structural Mechanics

E-mail: *cjsmec@challengejournal.com*

Web page: *cjsmec.challengejournal.com*

TULPAR Academic Publishing
www.tulparpublishing.com

Challenge Journal of Structural Mechanics

CONTENTS

Research Articles

TULPAR ACADEMIC PUBLISHING

Challenge Journal of Structural Mechanics

Research Article

Optimum design of a vaulted roof steel structure using grey wolf and backtracking search optimization algorithms through application programming interface

Osman Tunca [a,*]

[a] *Department of Civil Engineering, Karamanoğlu Mehmetbey University, 70200 Karaman, Turkey*

ABSTRACT

In present study, structural formation identification of a vaulted roof steel structure is taken as optimization problem. The cost of a steel structure is directly related to the weight of the structure. Weight minimization of the vaulted roof steel structure is considered as objective function of the design problem. The design problem is intended to be as realistic as possible. Wind loads and snow loads are calculated in direction of TS EN 1991-1-4 and TS EN1991-1-3practice code specifications, respectively. And dead loads reobtained in terms of gravity. The structural design constraints of the optimization problem are determined according to American Institute of Steel Construction-Allowable Stress Design (AISC-ASD). In the design, W-shaped steel profile sections to be selected for assigning to the structural elements are considered as discrete design variables. Grey Wolf Optimizer (GWO) and Backtracking Search Optimization (BSO) algorithms that are relatively recent metaheuristic algorithms are utilized as optimizer tools to obtain the minimum weighted structural design. The vaulted roof steel structure is initially modeled in a finite element packaged software (ANSYS Workbench v18.1). Then, using the application programming interface of the software, integration of finite element model with GWO and BSO optimization algorithms encoded in Microsoft Visual Basic for Application (MS VBA v7) programming language is provided. Thus, the performances of two new generation optimization algorithms in design optimization of a vaulted roof steel structure are compared and the benefits of the application programming interface are demonstrated.

ARTICLE INFO

Article history:
Received 30 November 2021
Revised 6 January 2022
Accepted 24 January 2022

Keywords:
Vaulted roof steel structures
Design optimization
Finite element analysis
Grey wolf optimizer
Backtracking search optimization

1. Introduction

Nowadays, it has become more significant to design long-span structure with low costs in the construction sector due to the scarcity of raw material resources. A vaulted roof steel structure stands out with its cost and construction speed (Wu et al., 2020). Additionally, this type of structure presents lightweight roof systems to reduce self-weight of the steel structure (Pavic et al. 2002). In the building sector, the vaulted roof steel structures are used various fields such as canopy roofs (Natalini et al. 2013), greenhouses (Demetres et al. 2016), factory buildings, etc. and they are also used in the most of long-span structures (Hamdy et al. 2018).

The structural engineers are currently faced with many complicated engineering design problems and that means confrontation a lot of mathematical operations. This becomes more complex when the material and geometric non-linearity and the many details of the practice provisions are added to the operations. Finite element analysis (FEA) packaged software are often used to overcome this complexity. These software shave developed considerably in recent years. They are used for simulation of the designing structures. So, these FEA packaged softwares help the structural engineers before site construction. But, in the pre-design phase, the trial-and-error method is commonly used by structural design engineers to decide the sizes of load carrying structural ele-

* *Corresponding author*. Tel.: +90-338-226-2200 ; Fax: +90-338-226-2214 ; E-mail address: osmantunca@kmu.edu.tr (O. Tunca)
ISSN: 2149-8024 / DOI: https://doi.org/10.20528/cjsmec.2022.01.001

ments. This is not enough for yielding an optimum structure in such a complex design problem since the decided variables affect each other in a structural design.

An optimum design is to find the most suitable design simultaneously considering design variables and design constraints. It consists of three main parts such as objective function, design variables, and design constraints. In a steel structure design, the objective of the design problem is generally cost of the structure. And this is directly related to weight of the steel structure. The design variables may be any dimension of the structure and/or cross sections of the structural members. The design constraints of such a design problem come from the provisions of code specifications and practicality.

There are various kinds of optimization methods. These are basically divided into two main groups such as deterministic and probabilistic (stochastic) optimization methods. The deterministic methods contain many complex mathematical operations such as gradients. Since a structural optimization problem to be solved is already quite complex, the probabilistic methods come to the forefront in this case. But it cannot be claimed that the designs obtained from probabilistic optimization algorithms based on randomness are exact optimum. But there is a great variety of design problems in which they cannot be solved via deterministic methods (Carbas et al. 2021).

Stochastic optimization methods are developed day by day. Both existing optimization algorithms are developed, and new generation algorithms are emerged. In the literature, it is seen that these algorithms increase their popularity with classical algorithms such as particle swarm optimization algorithm (PSO) (Kennedy and Eberhart 1995), harmony search algorithm (HSA) (Woo et al. 2001) and genetic algorithm (GA) (Goldberg and Holland 1988). The new generation algorithms such as African vultures optimization algorithm (Abdollahzadeh et al. 2021), honey badger algorithm (Hashim et al. 2022), rain optimization algorithm (ROA) (Moazzeni and Khamehchi 2020), new caledonian crow learning algorithm (Al-Sorori and Mohsen 2020), etc. have been added to these in the last decades. In addition, new versions of old algorithms are also emerging (Ponz-Tienda et al. 2017; Huang and Chen 2020; Postolov and Iliev 2022; Chakraborty et al. 2021; Khan and Ling 2021).

In the optimization process, encoding of a complex optimization problem is time consuming. Stochastic optimization algorithms operate the objective function as it is. The derivatives of the function are not needed. Therefore, the full expression of the objective function is not required. It is sufficient to only get the outputs of the function for stochastic optimization. Many FEA-based packaged software present their users access opportunity to application programming interfaces (API). So, the outputs that express the design purpose and can be obtained from the FEA packaged software can be used directly.

In this study, a vaulted roof steel structure is modeled via ANSYS Workbench v18.1 which is a famous FEA-based packaged software. Here, the snow loads and wind loads are considered TS EN 1991-1-3 and TS EN 1991-1-4 (2007), respectively. Besides, the ground acceleration is assigned in finite element method (FEM). Thus, the dead loads are considered as weight of the vaulted roof steel structure. The cross-sections of the four frame member groups are treated as design variables. The cross-sections of the frame elements are selected from the available profile list in AISC. Then, the grey wolf optimizer (GWO) and the backtracking search optimization (BSO) algorithms are encoded in Microsoft Visual Basic for Application (MS VBA v7). After then, the optimization algorithms are integrated in interface of the ANSYS Workbench v18.1 by using IRONPYTHON script. Thereby, a new and complex optimization design problem can be optimized with two novel metaheuristics. Thus, the designing of a vaulted roof steel structure is handled in detail using the API, and the performances of the two new optimization algorithms in obtaining minimum weight of a vaulted roof steel structure are compared and evaluated.

2. Design of a Vaulted Roof Steel Structure

The design of a vaulted roof steel structure having minimum structural design weight is taken into account as the objective of the optimization problem. This can be explained in more detail as follows.

Here, the I^T vector consists of steel sections of the vaulted roof steel structure. It includes N_d different section groups (Eq. (1)). Each member of the vector is represented as a sequence number of the steel sections as in the profile list.

$$I^T = \left[I_1, I_2, I_3, .., I_{N_d}\right] \tag{1}$$

The weight of the structure can be calculated by multiplying the volume of the structure and the unit weight as shown in Eq. (2).

$$W = \sum_{i=1}^{N_d} \rho_i A_i \sum_{j=1}^{N_t} L_j \tag{2}$$

Here, ρ_i is unit weight of the steel, A_i is the cross-section area of the steel profiles, N_t is the total number of the member in a group, and L_j is the length of each member.

Each member of the structure exposes to mechanic and geometric restrictions in design process. The mechanic limits can be given as follows.

$$\frac{(\delta_j - \delta_{j-1})}{h_j} \leq \delta_{ju} \quad j = 1,2,3,..,ns \tag{3}$$

Here, the inter-story drift of the structure stories should be limited with Eq. (3). The δ_j and δ_{j-1} are two lateral deflections of respective story, h_j is the story height, and δ_{ju} is the ultimate limit of the story drift ratio and ns is number of stories. Additionally, other displacements on the structure are limited using Eq. (4).

$$\delta_i \leq \delta_{iu} \qquad i = 1,2,3,..,nd \tag{4}$$

Here, nd is the total number of limited displacements. δ_i is the occurred deflection, andδ_{iu} is the upper bound

in the deflection. These may be horizontal column deflections or vertical beam deflections.

The shear capacities of the whole members of the structure are checked.

$$V_u \leq \varphi V_n \tag{5}$$

Here, V_u is the required shear strength, φ is resistance factor in shear, V_n is nominal shear strength. Furthermore, combined stresses on the structural members are considered.

$$\left(\frac{P_u}{\varphi_c P_n}\right) + \left(\frac{8}{9}\frac{M_{ux}}{\varphi_b M_{nx}}\right) \leq 1 \quad \text{for} \quad \frac{P_u}{\varphi_c P_n} \geq 0.2 \tag{6}$$

$$\left(\frac{P_u}{2\varphi_c P_n}\right) + \left(\frac{M_{ux}}{\varphi_b M_{nx}}\right) \leq 1 \quad \text{for} \quad \frac{P_u}{\varphi_c P_n} \leq 0.2 \tag{7}$$

In Eqs. (6) and (7), P_u is applied axial load, P_n is nominal axial strength, φ_c is resistance factor in compression, φ_b is resistance factor in bending, M_{ux} is applied moment, and M_{nx} is nominal flexural strength. The two W-shaped steel sections are intertwined in some connections of the frame. Finally, the flange width of the beam section (B_{jb}) should be equal or less than the flange width of column section (B_{jc}).

$$B_{jb} \leq B_{jc}, \quad j = 1,2,3, \dots, n \tag{8}$$

3. Calculation of Wind and Snow Loads

In this study, in order to determine the wind and snow loads, the TS EN 1991-1-4 and TS EN-1991-1-3 are considered, respectively.

3.1. Wind loads

The basic wind velocity is calculated considering directional factor C_{dir} and season factor C_{season}. The values of both are recommended as 1.0.

$$V_b = C_{dir} C_{season} V_{b,0} \tag{9}$$

The mean wind velocity $V_m(z)$ is obtained using the basic wind velocity V_b as Eq. (10).

$$V_m(z) = C_r(z) C_0(z) V_b \tag{10}$$

In here, $C_o(z)$ is the orography factor. Recommended value of this factor is 1.0. $C_r(z)$ is roughness factor. It can be calculated using Eq. (11).

$$C_r(z) = k_r \, ln\left(\frac{z}{z_0}\right) \quad \text{for} \quad z_{min} \leq z \leq z_{max}$$

$$C_r(z) = C_r(z_{min}) \quad \text{for} \quad z \leq z_{min} \tag{11}$$

In Eqs. (11) and (12), z is the height of the structure. Here, four different terrain categories are considered. The value of z_0 and $z_{\min}$ are determined using Table 1. $z_{\max}$ is taken as 200m for all terrain categories. k_r is terrain factor depending on z_0. It can be calculated as follow.

$$k_r = 0.19 \left(\frac{z_0}{z_{0,II}}\right)^{0.07} \tag{12}$$

The standard deviation of the turbulence σ_v is obtained via Eq. (13).

$$\sigma_v = k_r V_b k_l \tag{13}$$

Here, it is recommended to take the turbulence factor k_l as 1.0. The turbulence intensity $I_v(z)$ can be calculated using Eq. (14).

$$I_v(z) = \frac{\sigma_v}{V_m(z)} = \frac{k_l}{C_0(z)\, ln\left(\frac{z}{z_0}\right)} \quad \text{for} \quad z_{min} \leq z \leq z_{max}$$

$$I_v(z) = I_v(z_{min}) \quad \text{for} \quad z \leq z_{min} \tag{14}$$

Then, the peak velocity pressure $q_p(z)$ is determined via Eq. (15).

$$q_p(z) = [1 + 7I_v(z)]\frac{1}{2}\rho V_m^2 \tag{15}$$

Finally, wind pressure on the surface w_e depending on the pressure coefficient C_{pe} is calculated using Eq. (16). The wind pressure acting on the internal surfaces w_i of the structure can also be calculated by Eqs. (16) and (17).

$$w_e = q_p(z_e) C_{pe} \tag{16}$$

$$w_i = q_p(z_i) C_{pi} \tag{17}$$

Table 1. Terrain categories and terrain parameters (EN 1991-1-4).

Terrain category	Descriptions	z_0 (m)	$z_{\min}$ (m)
0	Sea or coastal area exposed to the open sea	0.003	1
1	Lakes or flat and horizontal area with negligible vegetation and without obstacles	0.01	1
2	Area with low vegetation such as grass and isolated obstacles (trees, buildings) with separations of at least 20 obstacle heights	0.05	2
3	Area with regular cover of vegetation or buildings or with isolated obstacles with separations of maximum 20 obstacle heights (such as villages, suburban terrain, permanent forest)	0.3	5
4	Area in which at least 15 % of the surface is covered with buildings and their average height exceeds 15 m	1	10

The calculation on the wind load of the circular cylindrical roof and domes is given in TS EN 1991-1-4, in section 7. Here, the roof is divided into four equal surfaces. The first of these parts is called A, the second and third surfaces are called B, and the last is called C. Wind loads on all parts are calculated using $C_{pe,10}$ coefficients from the Fig. 1. In here, f is height of the roof, h is the height of the columns and d is the span of the roof.

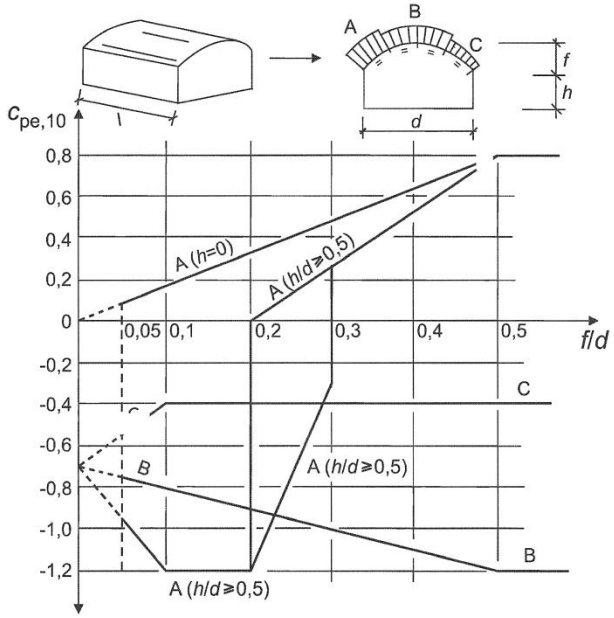

Fig. 1. The external pressure coefficients of $C_{pe,10}$ recommended for rectangular based vaults (EN 1991-1-4).

The wind pressure on the vertical wall of rectangular plan buildings is considering as given in section 7 in TS EN-1991-1-4.

3.2. Snow loads

In Eurocode (EN 1991-1-3), snow loads on the roof are calculated using Eq. (18).

$$S = \mu_i C_e C_t S_k \tag{18}$$

Here, S is snow load, μ_i is shape coefficient, C_e is exposure coefficient and C_t is thermal coefficient. S_k is the characteristic value of snow load on the ground. For some glass covered roofs, the snow load is reduced because of melting caused by heat loss. For other cases C_t is considered as 1.0. C_e can be specified depending on topology or, it can be taken as 1.0. To determine snow load on the cylindrical roof, drift case is considered. In Fig. 2, case (i) and case (ii) represent the undrifted and drifted load arrangement, respectively. In this study, undrifted load arrangement is considered. Finally, S_k can be determined via Attachment-E.

4. Stochastic Optimization Techniques

In this study, to design vaulted roof steel structure two novel optimization algorithms are used. Thus, the performance of grey wolf optimizer (GWO) and backtracking search optimization algorithm (BSOA) on a vaulted roof steel structure are investigated. Additionally, obtained performances in finding the minimum structural weight are compared and evaluated.

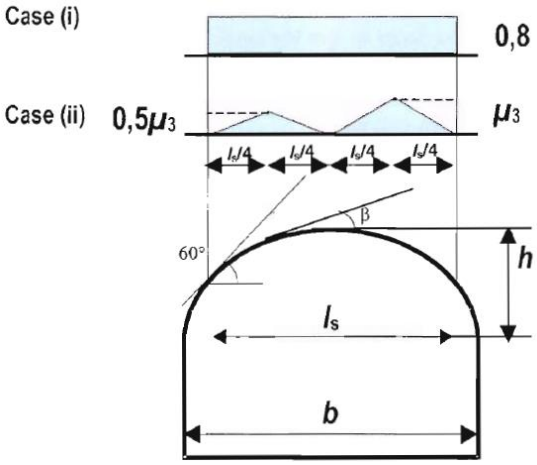

Fig. 2. The shape coefficients of the cylindrical roof.

4.1. Grey wolf optimizer (GWO)

Grey wolf optimizer was developed by Mirjalili et al. (2014) inspiring behaviors of grey wolves (Canis lupus). They hunt the preys as a group and, these animals have a hierarchy. There are three dominant grey wolf named alpha (α), beta (β) and omega (ω) in the hierarchical structure. The most dominant one is the alpha.

Hunters who hunt in groups surround their prey at the beginning of the hunt. The encircling behavior of grey wolves is represented by Eqs. (19) and (20).

$$\vec{D} = \left|\vec{C}\vec{X}_p(t) - \vec{X}(t)\right| \tag{19}$$

$$\vec{X}(t+1) = \vec{X}_p(t) - \vec{A}\vec{D} \tag{20}$$

Here, t is the number of iterations. $\vec{X}$ and $\vec{X}_p$ are the positions of grey wolves and prey, respectively. $\vec{A}$ and $\vec{C}$ are the coefficient vectors given in following equations.

$$\vec{A} = 2\,\vec{a}\vec{r}_1 - \vec{a} \tag{21}$$

$$\vec{C} = 2\,\vec{r}_2 \tag{22}$$

In Eqs. (21) and (22), $\vec{r}_1$ and $\vec{r}_2$ are randomly generated vectors. They are between 0 and 1. $\vec{a}$ is linearly reduced 2 to 0 during the iterative process.

The hunting begins after the prey or preys encircled. The alpha, most dominant gray wolf, leads the hunt. But sometimes beta and gamma also have an effect. So, the locations of all grey wolves are repositioned according to the top three best results. For this purpose, following equations are operated.

$$\vec{D}_\alpha = \vec{C}_1\vec{X}_\alpha - \vec{X},\ \vec{D}_\beta = \vec{C}_2\vec{X}_\beta - \vec{X},\ \vec{D}_\delta = \vec{C}_3\vec{X}_\delta - \vec{X} \tag{23}$$

$$\vec{X}_1 = \vec{X}_\alpha - \vec{A}_1(\vec{D}_\alpha),\ \vec{X}_2 = \vec{X}_\beta - \vec{A}_2(\vec{D}_\beta),\ \vec{X}_3 = \vec{X}_\delta - \vec{A}_3(\vec{D}_\delta) \quad (24)$$

$$\vec{X}(t+1) = \frac{\vec{X}_1 + \vec{X}_2 + \vec{X}_3}{3} \quad (25)$$

The grey wolves complete the hunt by attacking after they stop the repositioning. Here, the $\vec{A}$ starts to decrease due to the decrease in $\vec{a}$. This forces the gray wolves to attack.

4.2. Backtracking search optimization algorithm (BSOA)

Civicioglu (2013) studied on a novel metaheuristic algorithm named backtracking search optimization (BSO) algorithm. BSOA consists of five main processes named initialization, selection-I, mutation, crossover, and selection-II. In initialization, initial parameters are entered into the algorithm such as population size, number of dimensions of problem, lower and upper bounds of search spaces est. Then, initial population is generated as in Eq. (26).

$$P_{i,j} \sim U(\text{low}_j, \text{up}_j) \quad (26)$$

Here, U represents uniform probability distribution and, each $P_{i,j}$ in the population P is possible solution value.

In the selection-I, historical population P_{old} is determined. When P_{old} is first defined, it is randomly generated, as in P. Then, Eq. (27) is used for the following iterations.

$$\text{if } a < b \quad \text{then} \quad \text{old}P := P|a, b \sim U(0,1)| \quad (27)$$

In Eq. (27), a and b are random value between 0 and 1. If a is smaller than b, member of P_{old} is changed with member of P. Else, value of P_{old} is saved as memory of BSOA. Then, the order of the individuals in P_{old} is randomly changed via Eq. (28).

$$\text{old}P := \text{Permuting}(\text{old}P) \quad (28)$$

In the mutation process, first form of the trial population Mutant is determined using Eq. (29).

$$\text{Mutant} = P + F\ (\text{old}P - P) \quad (29)$$

Here, F is a coefficient that adjusts the amplitude of the search direction. It may be generated randomly in each iteration. The final form of the trial population T is generated in crossover stage. The crossover process consists of two main stages. In the first, the binary integer-valued matrix (map) is randomly generated. Its elements are the values 0 and 1. The matrix dimensions of the *map* are same as T and P. If the member of *map* is equal to 1.0, the member of T is manipulated via the relevant member of P in same numbered row and column. After that, each member of T is checked to ensure that its value between upper and lower boundaries. In case the values exceed the limits, boundary values are assigned instead of these values.

In selection-II, global minimum value is checked. If the *global minimum value* that saved is worse than the fitness of best individual of P (P_{best}). The best fitness value of the P is assigned to the *global minimum value* in memory.

5. Application Programming Interface (API)

Many structural optimization problems can be modeled by the matrix-displacement method. In structural design problems, it is very important that the obtained designs are as realistic and practicable as possible. The structural design problems become so complex when material nonlinearity, geometric nonlinearity, specification provisions, and serviceability are considered.

There are many finite elements (FE) based packaged software based on the matrix-displacement method that are frequently used in the construction industry. This is why the building simulations through these are easy. Additionally, some FE-based packaged software allow to connect interface of the software via commonly used programming languages.

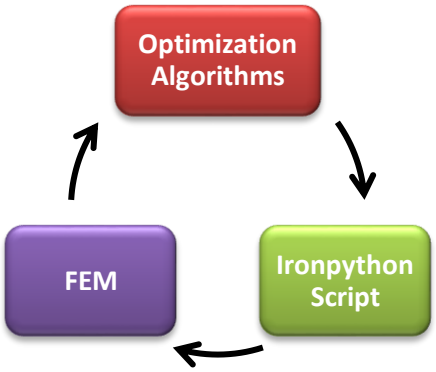

Fig. 3. Interaction between finite element model (FEM) and optimization algorithms via IRONPYTHON script.

In this study, the API functions of ANSYS Workbench v18.1 is used to connect it with the BSOA and GWO algorithms which are encoded in MS VBA 7. To make this, IRONPYTHON script is utilized as seen Fig. 3. Thus, optimum design information is transferred to FEM-based ANSYS as inputs and, the results of FEM analysis obtained from ANSYS are given as outputs.

6. Design Example

The minimum weighted design of a vaulted roof steel structure is considered as design example of this study. The heights of the column elements are 10m and the total height of the structure is 12m. The spans of the beams are 20m and the total length of the structure is 40m. The spans of the roof purlins and the wall purlins are 10m. The design variables of the optimization problem are the cross-sections of the structural members. All members are divided in to four different member groups. These are the columns, the beams, the wall purlins, and the roof purlins. In Fig. 4(a), each of these is depicted by different colors. The thicknesses of the roof and sidewall panels

shown in Fig. 4(b) are considered as 1mm steel sheet. The maximum mesh size is taken as 80cm. The quadrilateral method is used for surface meshing of the steel sheet. The finite element model of vaulted roof steel structure consists of totally 6410 nodes and 487 elements. In Fig. 4(c), the mesh distribution is seen.

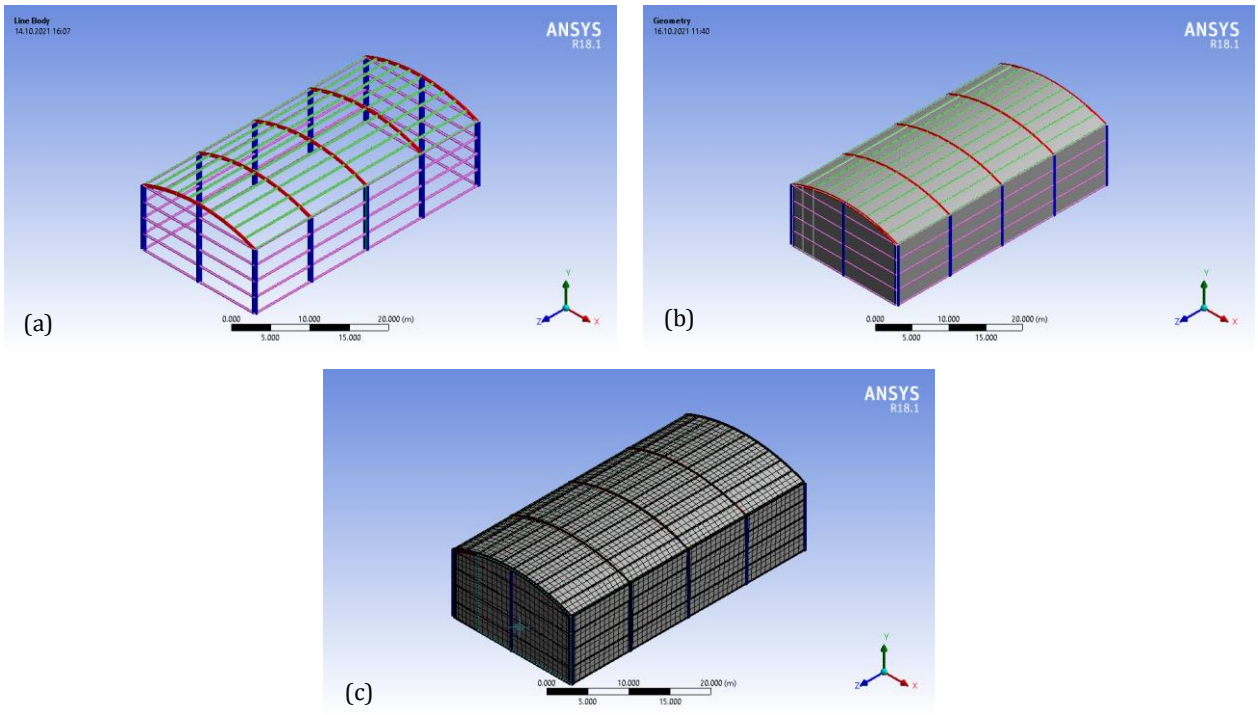

Fig. 4. The geometry, member groups and mesh distribution of the vaulted roof steel structure.

The snow and wind loads are subjected to the structure directly over the panels as in reality. The vaulted roof steel structure is modeled in ANSYS Workbenchv18.1. The entire structure is under the influence of gravity. So, the dead loads vary depending on the structural weight for each proposed design. The snow load acting on the roofis924 Pa according to provisions of TS EN 1991-1-3. The wind loads are determined considering the provisions of TS EN 1991-1-4. Thus, outer surface of the structure is divided into nine regions as shown in Fig. 5. All the wind loads acting on these regions are tabulated in Table 2.

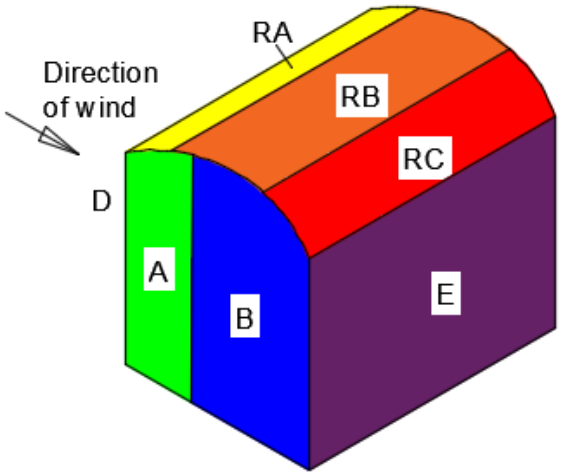

Fig. 5. Wind load regions of the vaulted roof steel structure.

Table 2. Wind loads acting on the regions of the vaulted roof steel structure.

Wind loads on side		Wind loads on the roof	
Name	Wind load	Name	Wind load
A	1452 Pa	RA	1742 Pa
B	871 Pa	RB	1162 Pa
D	649 Pa	RC	581 Pa
E	281 Pa		

In the optimization process, the GWO and BSO algorithms are used as optimizer tools of this study abovementioned in Section 4. The population sizes of both metaheuristic algorithms are considered as 7. The obtained optimal design results are presented in Table 3. Additionally, integer number of the W-sections are given in parenthesis. It is clear from this table that the BSO algorithm yields the minimum weighted structure with design weight of 78.604 ton. The GWO acquires slightly heavier structural design than BSO with design weight of 78.77 ton. The difference between optimal structural design weights yielded via GWO and BSO algorithms is only 0.21%. This proves that the algorithmic performances of both algorithms are almost similar for this design example. Additionally, it is seen from the Table 3 that the stress constraints are not effective for this structural design problem, instead the vaulted roof steel structure is sized according to the displacement limiters.

Table 3. The obtained optimum results.

	Number of cycle	Assigned section to columns	Assigned section to beams	Assigned section to roof purlins	Assigned section to wall purlins	Weight (ton)	Stress ratios	X-def$_{max}$ (m)	Z-def$_{max}$ (m)	Y-def$_{max}$ (m)
BSO	159	W530x82 (137)	W410X100 (168)	W310x21 (242)	W310x28.3 (240)	78.604	0.587	0.020	0.011	0.049
GWO	424	W530x72 (138)	W460x89 (159)	W310x21 (242)	W310x500 (213)	78.766	0.596	0.020	0.012	0.050

The maximum iteration number which can be identified as the maximum needed structural analysis is taken as 1000 for both algorithms. But the BSO and GWO algorithms accomplished the optimum designs in 159th and 424th iterations, respectively. So, it can be concluded that the BSO algorithm needs less computational effort. In design history graph as shown in Fig. 6, it is enough to present feasible design weights obtain in the first 500 iterations. Furthermore, it is obviously seen from this figure that although the BSO algorithm revealed worse performance in the earliest phases of the optimization process, it ended with lighter design as final.

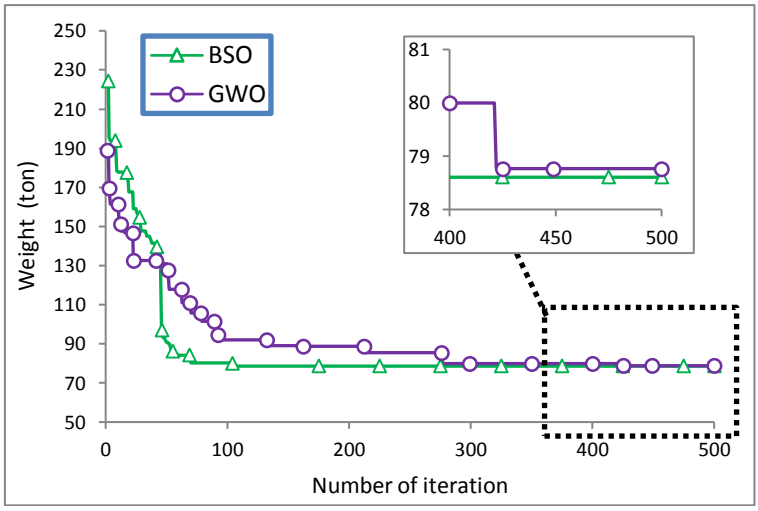

Fig. 6. The minimization performance of the BSO and GWO.

7. Conclusions

In this study, the design optimization of a vaulted roof steel structure to obtain minimum structural weight is considered as an optimization problem. The cross-sections of the roof purlins, the wall purlins, the beams and the columns are treated as design variables of this problem. They are taken into account as discrete design variables and, The W-shaped steel profiles are selected from available list of American Institute of Steel Construction (AISC). The encoded optimization algorithms are supplied with structural responses in virtue of a finite element method (FEM) based software integrated through application programming interface. (API). Thus, the vaulted roof steel structure is modelled in ANSYS Workbench v18.1. It is subjected to wind and snow loads as well as the dead loads. The TS EN 1991-1-4 and TS EN.1991-1-3 provisions are used to determine the wind and snow loads, respectively. The gravity is directly assigned to FEM for defining the dead load. The structural design constraints of optimization problem are considered using the limitations of AISC-ASD. The Grey Wolf Optimization (GWO) and Backtracking Search Optimization (BSO) algorithms, which are two novel metaheuristics, are encoded via Microsoft Visual Basic programming language to obtain the minimum weighted designs. The FEMs integrated to these algorithms utilizing the IRONPYTHON script file which are so-called the API functions.

This study leads to the following chief concluding remarks;

- The vaulted roof steel structures have an important role in the construction sector, especially in long-span structures.
- The GWO and BSO algorithms are primary used as design optimizer of such a structure in this study.
- Even the maximum number of structural analyses are taken as 1000, the BSO and GWO reaches the optimum designs in the 159th and 424th iterations, respectively. These verify that the BSO algorithms displays the most advantageous with respect to computational effort. Also, the BSO algorithm acquires the lightest vaulted roof steel structure, the those designed with the GWO algorithm has only 0.21% heavier design.
- The present findings confirm that thanks to the application programming interface (API), the optimum design problems can be handled in a very detailed way especially in having structural behavior responses more accurately.

Eventually, this study gives researchers an idea about how complex engineering design optimization problems can structurally be dealt by integrating optimization algorithms with the finite element method based software with aid of the application programming interface ability. As a future work, it is aimed to add the roof slope among the design variables. In this way, the structure can dynamically behave under acting loads, so the more realistic structural characteristics are taken into account in the design.

Acknowledgements

None declared.

Funding

The author received no financial support for the research, authorship, and/or publication of this manuscript.

Conflict of Interest

The author declared no potential conflicts of interest with respect to the research, authorship, and/or publication of this manuscript.

References

Abdollahzadeh B, Gharehchopogh FS, Mirjalili S (2021). African vultures optimization algorithm: A new nature-inspired metaheuristic algorithm for global optimization problems. *Computers & Industrial Engineering*, 158, 107408.

Aleksandar P and Reynolds P (2002). Vibration serviceability of long-span concrete building floors. Part 1: Review of background information. *Shock and Vibration Digest,* 34(3), 191-211.

Al-Sorori W, Mohsen AM (2020). New Caledonian crow learning algorithm: A new metaheuristic algorithm for solving continuous optimization problems, *Applied Soft Computing*, 92, 106325.

ANSI/AISC 341-16 (2016). Seismic provisions for structural steel buildings, American Institute of Steel Construction; Chicago, USA.

ANSYS Inc (2017). ANSYS Mechanical Theory Reference: Release 18.1. Canonsburg, PA, USA.

Briassoulis D, Dougka G, Dimakogianni D, Vayas I (2016). Analysis of the collapse of a greenhouse with vaulted roof, Biosystems Engineering, 151, 495-509.

Carbas S, Toktas A, Ustun D (2021) Nature-Inspired Metaheuristic Algorithms for Engineering Optimization Applications. Springer, Singapore.

Chakraborty S, Saha AK, Nama S, Debnath S (2021). COVID-19 X-ray image segmentation by modified whale optimization algorithm with population reduction, *Computers in Biology and Medicine*, 139, 104984.

Civicioglu P (2013) Backtracking search optimization algorithm for numerical optimization problems. *Applied Mathematics and Computation,* 219:8121–8144.

Goldberg DE, Holland JH (1988). Genetic algorithms and machine learning. *Machine Learning*, 3(2), 95–99.

Hamdy G, Kamal O, Al-Hariri O, El-Salakawy T (2018). Plane and vaulted masonry elements strengthened by different techniques – Testing, numerical modeling and nonlinear analysis. *Journal of Building Engineering*, 15, 203-217.

Hashim FA, Houssein EH, Hussain K, Mabrouk MS, Al-Atabany W (2022). Honey Badger Algorithm: New metaheuristic algorithm for solving optimization problems. *Mathematics and Computers in Simulation*, 192, 84-110.

Hotta H, Tsunoda T (2004a). An experimental study on influence of mullion-type wall of predominant bending failure in reinforced concrete frame. *Proceedings of the 1st International Conference on Urban Earthquake Engineering*, Yokohama, Japan, 105-111.

Hotta H, Tsunoda T (2004b). An experimental study on influence of mullion-type wall of predominant bending failure in load-carrying capacity and deformation efficiency of reinforced concrete frame. *Journal of Structural and Construction Engineering*, 582, 131-136 (in Japanese).

Huang YF, Chen PH (2020). Fake news detection using an ensemble learning model based on Self-Adaptive Harmony Search algorithms. *Expert Systems with Applications*, 159, 113584.

IronPython Team (2001-2020). Python Software Foundation. Microsoft Corporation, USA.

Kennedy J, Eberhart R (1995). Particle swarm optimization. *Proceedings of ICNN'95 - International Conference on Neural Networks*, 4, 1942-1948.

Khan TA, Ling SH (2021). A novel hybrid gravitational search particle swarm optimization algorithm. *Engineering Applications of Artificial Intelligence*, 102, 104263.

Microsoft Visual Basic Programming Language (2016). Microsoft Corporation One Microsoft Way Redmond, WA 98052-6399 USA.

Mirjalili S, Mirjalili SM, Lewis A (2014). Grey wolf optimizer. *Advances in Engineering Software*, 69, 46–61.

Moazzeni AR, Khamehchi E (2020). Rain optimization algorithm (ROA): A new metaheuristic method for drilling optimization solutions. *Journal of Petroleum Science and Engineering*, 195, 107512.

Natalini MB, Morel C, Natalini B (2013). Mean loads on vaulted canopy roofs. *Journal of Wind Engineering and Industrial Aerodynamics*, 119, 102-113.

Ponz-Tienda JL, Salcedo-Bernal A, Pellicer E, Benlloch-Marco J (2017). Improved Adaptive Harmony Search algorithm for the Resource Leveling Problem with minimal lags. *Automation in Construction*, 77, 82-92.

Postolov B, Iliev A (2022). New metaheuristic methodology for solving security constrained hydrothermal unit commitment based on adaptive genetic algorithm. *International Journal of Electrical Power & Energy Systems*, 134, 107163.

TS EN 1991-1-3 (2007). Eurocode 1: Actions on Structures - Part 1-3: General Actions - Snow loads.

TS EN 1991-1-4 (2007). Eurocode 1: Actions on Structures - Part 1-4: General Actions – Wind loads.

Woo Z, Hoon J, Loganathan GV (2001). A New Heuristic Optimization Algorithm: Harmony Search. *Simulation*, 76(2), 60-68.

Wu H, Liew A, Van Mele T, BlockT P (2020). Analysis and optimisation of a rib-stiffened vaulted floor for dynamic performance. *Engineering Structures*, 213, 110577.

Challenge Journal of Structural Mechanics

Research Article

Wind loads on girder bridges

Lyubomir A. Zdravkov [a,*]

[a] *Department of Metal, Wood and Plastic Structures, University of Architecture, Civil Engineering and Geodesy (UACEG), Sofia 1046, Bulgaria*

ABSTRACT

Bridges are facilities that are in exploitation outdoor. Often the wind is the leading horizontal force in the transverse direction. Therefore the bridges have received the due attention in the standards for wind loading. Unfortunately, in all available standards for wind load on the bridges, one, summarized value of the aerodynamic coefficient is indicated. It is related to the entire cross-section of the facility. There is no differentiation for the individual longitudinal girders and/or roadway. Information about the specific wind pressure on each of the bridge's element is required for the correct design of their supporting systems, whether they are framed or braced type. To fill this gap, the author has built several models of bridges with longitudinal girders, using a Computational Fluid Dynamics (CFD) analysis. Through them he determined the values of the aerodynamic coefficients for each of the bridge girders under the roadway and the cross-section of the bridge as a whole. Conclusions are summarized and the results clearly show the values of the aerodynamic coefficients for the whole section of the bridge are with 50-60% lower than the ones reported for the windward girder.

ARTICLE INFO

Article history:
Received 1 December 2021
Revised 19 January 2022
Accepted 1 February 2022

Keywords:
Wind
Load
Bridge
Longitudinal girder
Aerodynamic coefficient
CFD analysis

1. Introduction

Bridges are facilities that are in exploitation outdoor. Often the wind is the leading horizontal force in the transverse direction. Therefore in the following standards for loading on bridges AS/NZS 1170.2 (2011), BS 5400-2 (2006), EN 1991-1-4 (2005), IRC: 6-2017 (2017), Standards for Design of Road and Railway Bridges and Culverts (SDRRBC) (1989) and СП 35.13330.2011 (2011), the bridges have received due attention for wind impact. To increase the safety, the values of aerodynamic coefficients, specified in these standards, have been increased several times in comparison to those for buildings. However, the presented aerodynamic coefficients in the aforementioned standards are applicable to the entire sections of the bridges only. There is no separation and additional data by elements. Only in standard BS 5400-2 (2006) is written that the aerodynamic coefficient for assembled girders is 2.2, without taking into account any sheltering effect. Information about the wind load on each of the girders is required for the correct design of the supporting systems. One possible approach is to determine the aerodynamic coefficient for the whole section of the bridge and to use it separately for each of its elements. Another possible solution would be to look for some analogy with known facilities, such as long buildings or walls. But which of these approaches would produce more reliable results? And are they even close to the real wind load on bridges? To answer these questions, the author has built and researched several models of girder bridges, using Computational Fluid Dynamics (CFD) analysis. Based on these models, he determined the values of the aerodynamic coefficients for each one longitudinal girder under the roadway and for the cross-section of the bridge as a whole.

2. Model Description

Computational Fluid Dynamics (CFD) analysis is selected as a suitable approach to be used in the present study. Through the graphical interface Workbench of ANSYS (2020) and its module Fluid Flow (CFX) have

* *Corresponding author*. Tel.: +359-885-081-305 ; E-mail address: zdravkov_fce@uacg.bg (L. A. Zdravkov)
ISSN: 2149-8024 / DOI: https://doi.org/10.20528/cjsmec.2022.01.002

been created two general spatial models of bridge structures. In the first model the girders are with a rectangular cross section, by reinforced concrete. In the second model the girders are made of steel sheets. The height of all beams is 1,000 mm. The reinforced concrete beams are 400 mm wide, the steel ones - as is shown in Fig. 1b. Reinforced concrete slab with a thickness of 200 mm is placed above the girders there, see Fig. 1.

To increase the scope and usefulness of the study, the following sub-models have been created:

a) the number of beams under the slab n = 2, 3 and 4;

b) the distance between the beams x = 1, 2, 3, 4 and 5 m.

A spatial analysis is used in this paper. A typical cross-section of the bridge's structure is modelled in 2D and then extruded into a 6 m depth making an overall domain shape of a parallelepiped. Around the bridge structures are created box enclosure, see Fig. 3. The walls of the simulated wind tunnel around each bridge section are located at the following distances from them:

a) for bridges with two or three girders:

- fluid inlet - 5 m;
- fluid outlet - at 20 m, i.e. the body of the bridge is located much closer to the inlet of the wind tunnel, see Fig. 2;
- vertical sidewalls - as the "Symmetry" option is used, there is no distance between the walls and the cross-section of the bridge;
- horizontal walls (bottom and roof) - 10 m.

b) for bridges with four girders:

- fluid inlet - at 8 m;
- fluid outlet - at 32 m;
- vertical sidewalls - as the "Symmetry" option is used, there is no distance between them and the cross-section of the bridge;
- horizontal walls (bottom and roof) - 16 m.

The determining of the above-written distances between the walls of the virtual wind tunnel and bridge is based on the principle that airflow adjacent to the bridge should not affected, see Rusev et al. (2012a). Accepted distances are bigger than requirements of Tominaga et al. (2008), as follow:

- the top / bottom boundary should be set 5H or more away the obstacle, where H is the height of the bridge section in the current research (H = d = 1,200 mm, see Fig. 1);
- the outflow boundary should be set at least 10H behind the obstacle.

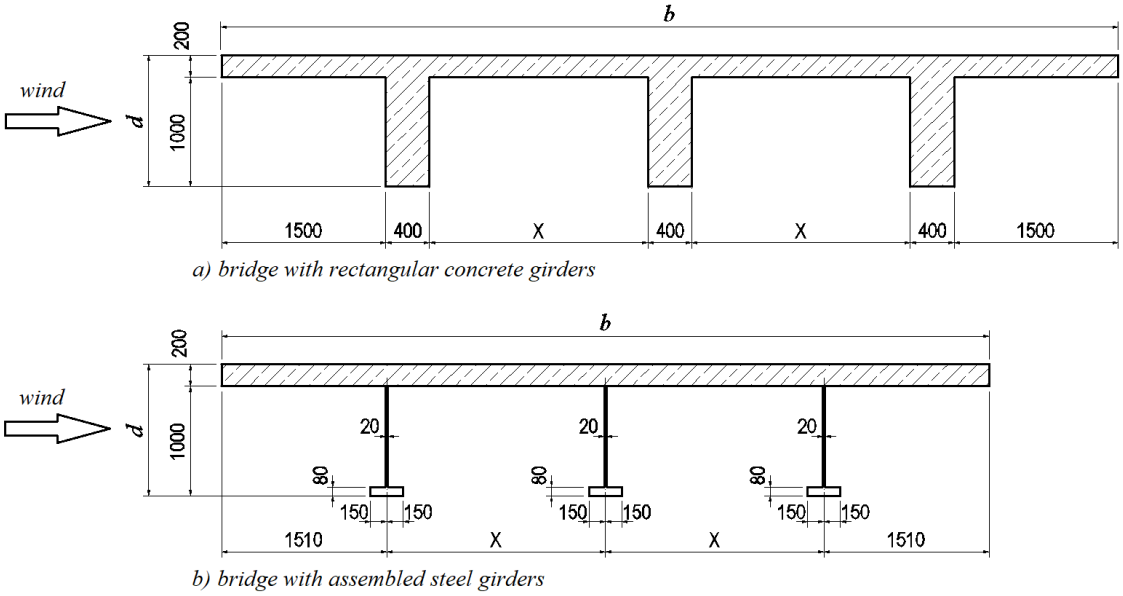

Fig. 1. Cross-sections of the researched bridges.

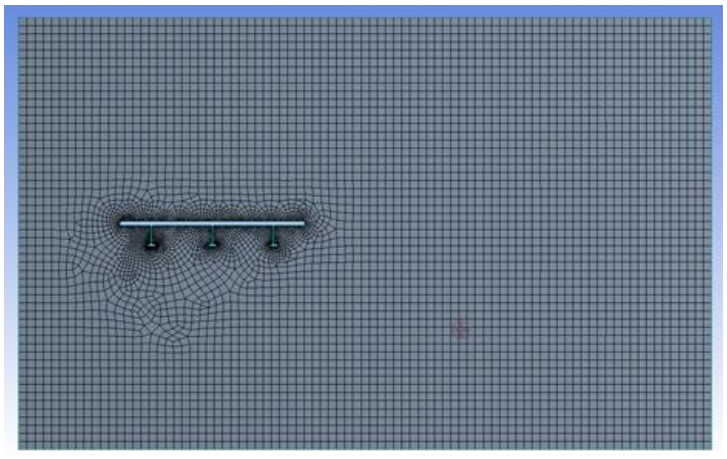

Fig. 2. Mesh refinement of the elements around the bridge.

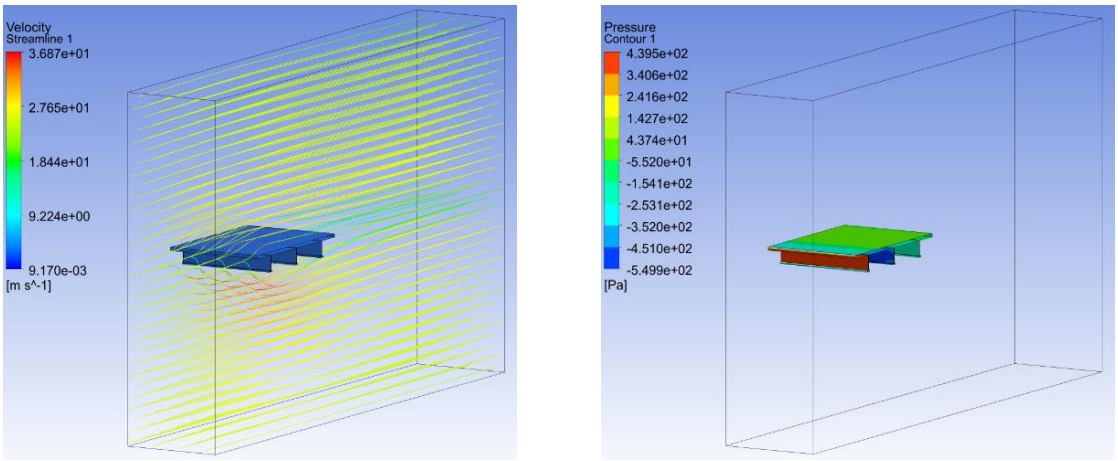

a) velocity of the wind flow around the bridge b) pressure on surfaces of the bridge elements

Fig. 3. Wind flow around the bridge and the resulting pressure on the elements.

At the same time, to avoid heavy computer solutions and save computational time, the maximum number of finite elements is maintained into reasonable limits. To optimize their mesh, it is significantly refined in the area around the bridge, see Fig. 2, and is sparse to the periphery, as is done in Rusev et al. (2012b). The maximum size of the finite elements of the air is limited to:

a) elements in direct contact with the slab and girders - 50 mm;

b) all other elements - 400 mm.

Another model with a denser mesh is created to check the sufficiency of the accepted mesh sizes. The maximum sizes of the finite elements there are twice as small as is written above – 25 mm for elements in direct contact and 200 mm for all other elements. The differences in resulting forces $F_{x,i}$ in the girders and the total aerodynamic coefficients $C_{cp,x}$ are less than 6%, i.e. accepted mesh has a good density.

When creating the mesh of finite elements, the "Quadratic" option is used, as a result of which the nodes in the middle of their sides are preserved. This type of element is characterized by its nonlinear deformation behaviour.

Steady state analysis type is used in a Fluid flow (CFX) module. K-ε model, part of Reynolds-averaged Navier Stokes (RANS) family, is used to simulate the turbulent flow of the fluid around the bridges. These RANS equations are an adequate representation of the wind tunnel's reality, Baklanov et al. (2007). Accepted turbulence has a medium (5%) intensity. No combustion and thermal radiation. The used fluid is an air ideal gas with a temperature of 25 °C. Its speed at the inlet domain of the tunnel is constant in height and has a value of v = 25 m/s. Flow regimes in outlet and opening domains are subsonic, with a relative pressure 0 Pa. Flow direction is normal to boundary conditions. Bridge section domain is no slip rough wall.

Unlike of the research of Mei Yu et al. (2011), there main wind flow is horizontal, i.e. the angle of attack is 0°. The direction of the approaching wind is perpendicular to the longitudinal axes of the bridge girders and deck.

The models of the bridge with rectangular reinforced concrete beams, see Fig. 1a, have roughness with a high of 0.5 mm on all surfaces. Models with steel girders, see Fig. 1b, have roughness with a height of 0.1 mm on all surfaces. The surface of the terrain under the bridge is perfectly smooth.

During its movement, the wind flows around the bridge, see Fig. 3a, which leads to the appearance of pressure on its elements, see Fig. 3b. As a result, generated in the bridge girders forces could be accounted for. Knowing the value of forces and area of the girders, the value of the total (whole) wind pressure on the girders can be determined by the formula:

$$q_{cp,x} = \frac{F_{x,i}}{A_g} \tag{1}$$

where $q_{cp,x}$ is the total (whole) pressure on the i-th bridge girder. It is equal to the sum of the conditionally positive (compression) and negative (suction) pressure on the girder; $F_{x,i}$ - the value of the accounted force on the i-th girder in the direction of the horizontal wind flow; A_g - the area of the i-th girder, transverse to the wind flow.

Reference mean (basic) velocity pressure q_b could be determined by the written in EN 1991-1-4 (2005) formula:

$$q_b = \frac{1}{2}\rho v_b^2 = \frac{1}{2} \cdot 1.25 \cdot 25^2 = 390 \text{ N/mm}^2 \tag{2}$$

where ρ = 1.25 kg/m^3 is the air density; v_b = 25 m/s – accepted wind speed in the current research.

The ratio of the total pressure $q_{cp,x}$ on the girders and the reference mean pressure q_b give us information about the value of the total aerodynamic coefficient $C_{cp,x}$ of the girders, i.e.:

$$C_{cp,x} = \frac{q_{cp,x}}{q_b} \tag{3}$$

3. Results

The values of the aerodynamic coefficients $C_{cp,x}$ for wind load in the horizontal plane, obtained by equations (1-3) are shown in:

a) Tables 1-3 for a bridge with rectangular reinforced concrete girders;

b) Tables 4-6 for a bridge with assembled steel girders.

Table 1. Total aerodynamic coefficient $C_{cp,x}$ for wind pressure on the elements of a bridge with two rectangular reinforced concrete beams.

x, m	1	2	3	4	5
b, m	4.8	5.8	6.8	7.8	8.8
b/d	4.0	4.833	5.667	6.5	7.333
$C_{cp,x,L}$	1.615	1.606	1.673	1.708	1.713
$C_{cp,x,R}$	-0.237	-0.309	-0.49	-0.65	-0.578
$C_{cp,x,tot}$	1.321	1.261	1.164	1.054	1.106

x - "clear" distance between the rectangular girders, see Fig. 1a
b - entire width of the bridge section
d = 1.2 m - the entire height of the cross-section of the bridge
$C_{cp,x,L}$ - total aerodynamic coefficient for the windward (left in this case) girder
$C_{cp,x,R}$ - total aerodynamic coefficient for the leeward (right here) girder
$C_{cp,x,tot}$ - total aerodynamic coefficient for the whole section of the bridge

Table 2. Total aerodynamic coefficient $C_{cp,x}$ for wind pressure on the elements of a bridge with three rectangular reinforced concrete beams.

x, m	1	2	3	4	5
b, m	6.2	8.2	10.2	12.2	14.2
b/d	5.167	6.833	8.5	10.167	11.833
$C_{cp,x,L}$	1.676	1.785	1.793	1.705	1.676
$C_{cp,x,m}$	-0.1573	-0.346	-0.482	-0.478	-0.533
$C_{cp,x,R}$	-0.205	-0.374	-0.340	-0.1209	0.1491
$C_{cp,x,tot}$	1.274	1.06	0.975	1.067	1.248

$C_{cp,x,m}$ - total aerodynamic coefficient for the middle girder

Table 3. Total aerodynamic coefficient $C_{cp,x}$ for wind pressure on the elements of a bridge with four rectangular reinforced concrete beams.

x, m	1	2	3	4	5
b, m	7.6	10.6	13.6	16.6	19.6
b/d	6.333	8.833	11.333	13.833	16.333
$C_{cp,x,L}$	1.547	1.675	1.603	1.570	1.501
$C_{cp,x,m,L}$	-0.076	-0.241	-0.268	-0.729	-0.498
$C_{cp,x,m,R}$	-0.174	-0.389	-0.455	-0.001	-0.013
$C_{cp,x,R}$	-0.174	-0.129	0.076	0.244	0.302
$C_{cp,x,tot}$	1.099	0.921	0.950	1.069	1.251

$C_{cp,x,m,L}$ - total aerodynamic coefficient for the left internal girder, in the direction of the wind flow
$C_{cp,x,m,R}$ – total aerodynamic coefficient for the right internal girder

Table 4. Total aerodynamic coefficient $C_{cp,x}$ for wind pressure on the elements of a bridge with two steel girders.

x, m	1	2	3	4	5
b, m	4.02	5.02	6.02	7.02	8.02
b/d	3.350	4.183	5.017	5.850	6.683
$C_{cp,x,L}$	1.610	1.664	1.773	1.803	1.798
$C_{cp,x,R}$	-0.086	-0.226	-0.560	-0.667	-0.683
$C_{cp,x,tot}$	1.422	1.372	1.160	1.078	1.090

x - axial distance between the steel girders, see Fig. 1b

Table 5. Total aerodynamic coefficient $C_{cp,x}$ for wind pressure on the elements of a bridge with three steel girders.

x, m	1	2	3	4	5
b, m	5.02	7.02	9.02	11.02	13.02
b/d	4.183	5.850	7.517	9.183	10.850
$C_{cp,x,L}$	1.632	1.832	1.929	1.844	1.795
$C_{cp,x,m}$	-0.041	-0.274	-0.672	-0.565	-0.512
$C_{cp,x,R}$	-0.133	-0.325	-0.308	-0.211	0.026
$C_{cp,x,tot}$	1.387	1.201	0.953	1.054	1.257

Table 6. Total aerodynamic coefficient $C_{cp,x}$ for wind pressure on the elements of a bridge with four steel girders.

x, m	1	2	3	4	5
b, m	6.02	9.02	12.02	15.02	18.02
b/d	5.017	7.517	10.017	12.517	15.017
$C_{cp,x,L}$	1.573	1.729	1.749	1.648	1.572
$C_{cp,x,m,L}$	-0.066	-0.153	-0.645	-0.623	-0.412
$C_{cp,x,m,R}$	-0.109	-0.266	-0.224	-0.103	-0.147
$C_{cp,x,R}$	-0.156	-0.293	0.077	0.194	0.262
$C_{cp,x,tot}$	1.189	1.002	0.953	1.089	1.230

When the value of the aerodynamic coefficient $C_{cp,x}$ is positive, it means that the equivalent force $F_{x,i}$ on the corresponding girder has the same direction of action as the wind flow. When $C_{cp,x}$ has a negative value, it means that the equivalent force $F_{x,i}$ has a direction of action opposite to the wind flow.

The change in the values of the aerodynamic coefficients $C_{cp,x}$, depending on the ratio b/d, is graphically shown in Fig. 4. Here it is noticeable that the equal force on the windward girders (left in these models) always has a direction coinciding with that of the wind flow. As a result, only positive values of the aerodynamic coefficient were accounted for, which are in the range $C_{cp,x,L}$ = 1.5-1.93. They are smaller than the value of the coefficient $C_{cp,x}$ = 2.2, specified in BS 5400-2 (2006), but bigger than the shown by Wassef (2016) value $C_{cp,x}$ = 1.3.

The equivalent force on the leeward girders (right in this case) can have a direction that is the same or opposite to that of the wind flow. The accounted values of the aerodynamic coefficient are in the range $C_{cp,x,R}$ = -0.68 ÷ 0.3.

The forces on the inner girders are always in the opposite direction to the wind flow. The reported values of the aerodynamic coefficient are $C_{cp,\,x,m}$ = -0.73-0.

The accounted values of the aerodynamic coefficient for the whole section of the bridge are only positive and are in the range $C_{cp,\,x,tot}$ = 0.92-1.4, i.e. they are smaller than the accounted for the windward girders.

The vertical force $F_{z,tot}$, which acts on the entire section of the bridge, was also taken into account in the study. Using the formulas (1-3), adapted for the vertical projection of the bridge, are determined the values of the generalized aerodynamic coefficients $C_{cp,z,tot}$ for the wind load in the vertical plane. They are shown in:

a) Tables 7-9 for a bridge with rectangular reinforced concrete beams;

b) Tables 10-12 for a bridge with assembled steel beams.

Table 7. Total aerodynamic coefficient $C_{cp,z,tot}$ for wind pressure on the elements of a bridge with two rectangular reinforced concrete girders.

x, m	1	2	3	4	5
b, m	4.8	5.8	6.8	7.8	8.8
b/d	4.0	4.833	5.667	6.50	7.333
$F_{z,tot}$, kN	8.033	5.991	2.910	-1.085	-4.681
$C_{cp,z,tot}$	0.715	0.441	0.183	-0.059	-0.227

$F_{z,tot}$ - vertical force, generated by the wind flow acting on the whole section of the bridge;
$C_{cp,z,tot}$ - total aerodynamic coefficient in the vertical plane for the whole section of the bridge

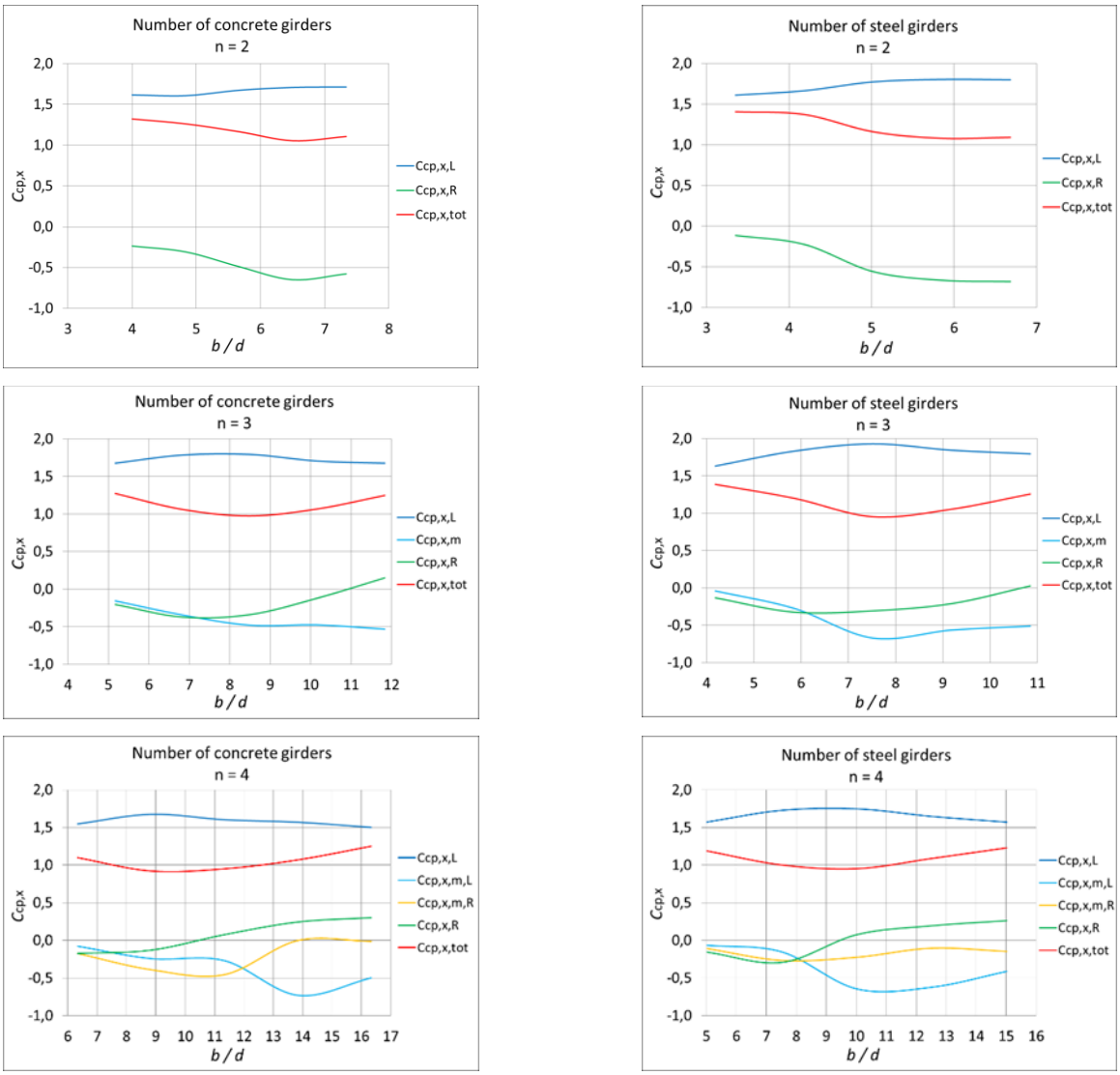

a) for rectangular concrete girders b) for steel girders

Fig. 4. Values of the coefficient $C_{cp,x}$ in relation with the ratio b/d.

Table 8. Total aerodynamic coefficient $C_{cp,z,tot}$ for wind pressure on the elements of a bridge with three rectangular reinforced concrete girders.

x, m	1	2	3	4	5
x, m	1	2	3	4	5
b, m	6.20	8.20	10.20	12.20	14.20
b/d	5.167	6.833	8.5	10.167	11.833
$F_{z,tot}$, kN	5.873	-0.514	-5.717	-7.117	-5.609

Table 9. Total aerodynamic coefficient $C_{cp,z,tot}$ for wind pressure on the elements of a bridge with four rectangular reinforced concrete girders.

x, m	1	2	3	4	5
b, m	7.6	10.6	13.6	16.6	19.6
b/d	6.333	8.833	11.333	13.833	16.333
$F_{z,tot}$, kN	3.332	-3.846	-5.413	-1.873	-1.775
$C_{cp,z,tot}$	0.187	-0.155	-0.170	-0.048	-0.039

Table 10. Total aerodynamic coefficient $C_{cp,z,tot}$ for wind pressure on the elements of a bridge with two steel girders.

x, m	1	2	3	4	5
b, m	4.02	5.02	6.02	7.02	8.02
b/d	3.350	4.183	5.017	5.850	6.683
$F_{z,tot}$, kN	9.702	7.472	3.170	-0.089	-4.455
$C_{cp,z,tot}$	1.031	0.636	0.225	-0.005	-0.237

Table 11. Total aerodynamic coefficient $C_{cp,z,tot}$ for wind pressure on the elements of a bridge with three steel girders.

x, m	1	2	3	4	5
b, m	5.02	7.02	9.02	11.02	13.02
b/d	4.183	5.850	7.517	9.183	10.850
$F_{z,tot}$, kN	8.545	1.960	-4.381	-6.321	-6.129
$C_{cp,z,tot}$	0.727	0.119	-0.208	-0.245	-0.201

Table 12. Total aerodynamic coefficient $C_{cp,z,tot}$ for wind pressure on the elements of a bridge with four steel girders.

x, m	1	2	3	4	5
b, m	6.02	9.02	12.02	15.02	18.02
b/d	5.017	7.517	10.017	12.517	15.017
$F_{z,tot}$, kN	6.148	-1.920	-2.698	-2.547	-2.623
$C_{cp,z,tot}$	0.4364	-0.0910	-0.0959	-0.0725	-0.0622

When the value of the aerodynamic coefficient $C_{cp,z,tot}$ is positive, it means that the equivalent force $F_{z\,tot}$ on the bridge has a bottom-up direction. When $C_{cp,z,tot}$ has a negative value, it means that the equivalent force $F_{z,tot}$ has a top-down direction, i.e. coinciding with the gravity.

The change in the values of the aerodynamic coefficients $C_{cp,z,tot}$, depending on the ratio b/d, is graphically shown in Fig. 5 where $C_{cp,z,2}$, $C_{cp,z,3}$, $C_{cp,z,4}$, are the total coefficients for pressure when the number of girders under the plate is n = 2, 3 and 4 pcs.

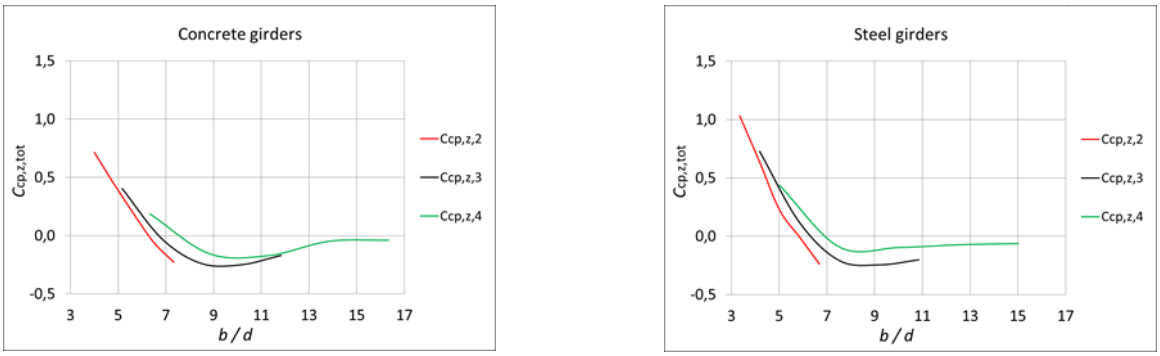

a) for rectangular concrete girders b) for steel girders

Fig. 5. Values of the coefficient $C_{cp,z,tot}$ in relation with the ratio b/d

It is noteworthy here that at small values of the ratio b/d, the equivalent vertical force $F_{z,tot}$ acts from the bottom-up direction. The maximum value of the total aerodynamic coefficient accounted here is $C_{cp,z,tot}$ = 1.1. At higher values of the ratio b/d, the equal vertical force $F_{z,tot}$ acts from top to bottom, i.e. wind loads have the same direction as gravitational ones. Values of the total aerodynamic coefficient accounted here are of the order of $C_{cp,z,tot}$ = -0.24. It can be seen that there is a difference with the value of $C_{cp,z,tot}$ = ± 0.9, recommended in EN 1991-1-4 (2005).

4. Conclusions

In widespread standards for loading on bridges does not exist information about wind loading on the individual elements. For their determination, through the graphical interface Workbench of ANSYS (2020) and its

module for computational fluid dynamics Fluid Flow (CFX) are researched several typical bridge sections with longitudinal girders. From the conducted study the following conclusions could be drawn:

- The windward beams are the heaviest loaded by the wind flow;
- The total load on the leeward girders may have a direction that coincides with or is opposite to that of the wind flow. The reference aerodynamic coefficients are two to three times smaller than those for the windward girders;
- The total load on the internal girders is always in the opposite direction to the wind flow;
- The reported values of the aerodynamic coefficient for the whole section of the bridges are only positive and are with 50-60% lower than the ones reported for the windward girders. And if they are used for measurement of the stabilizing elements of the girders, it would be in the direction of uncertainty;
- In addition to forces in their plane, horizontal wind flows also cause forces in the vertical direction. Which forces in narrow bridges are unloading, but in wide ones, they are superimposed with gravitational loads.

Acknowledgements

The author would like to express his gratitude to eng. Maria Pantusheva, for the carefully reading of the article and clever advices in CFD analysis.

Funding

The author received no financial support for the research, authorship, and/or publication of this manuscript.

Conflict of Interest

The author declared no potential conflicts of interest with respect to the research, authorship, and/or publication of this manuscript.

References

ANSYS® v.2020 R2 (2020). Documentation. Ansys Inc., Canonsburg, PA, USA.

AS/NZS 1170.2 (2011). Structural Design Actions. Part 2: Wind actions. Standards Australia Limited / Standards New Zealand. ISBN 978-0-7337-9805-4.

Baklanov A, Barmpas P, Bartzis J, Batchvarova E et al. (2007). Best practice guideline for the CFD simulation of flows in the urban environment. COST Action 732, Brussels, Belgium.

BS 5400-2 (2006). Steel, Concrete and Composite Bridges – Part 2: Specifications for Loads. British Standards Institution.

СП 35.13330.2011 (2011). Bridges and culverts. Ministry of Regional Development, Russian Federation, Moscow.

EN 1991-1-4:2005+A1:2010 (2005). Eurocode 1: Actions on structures – Part 1-4: General actions – Wind actions. European Committee for Standardization, Brussels.

IRC: 6-2017 (2017). Standard Specifications and Code of Practice for Road Bridges. Section: II – Loads and Load Combinations (Seventh Revision). Indian Road Congress.

Rusev I, Dinev D, Tanev T (2012b). Numerical study of wind actions on nearby tall buildings. *International Jubilee Scientific Conference UACEG'2012*, Sofia, 15-17 (on Bulgarian).

Rusev I, Tanev T, Dinev D (2012a). Numerical study of wind actions on tall buildings with ANSYS CFX and comparison with EN1991-1-4. *XII International Scientific Conference VSU'2012*, Sofia, vol. 1, 83-88. (in Bulgarian)

Standards for Design of Road and Railway Bridges and Culverts (1989). КТСУ, Sofia.

Tominaga Y, Mochida A, Yoshie R, Kataoka H, Nozu T, Yoshikawa M, Shirasawa T (2008). AIJ guidelines for practical applications of CFD to pedestrian wind environment around buildings. *Journal of Wind Engineering and Industrial Aerodynamics*, 96(10-11), 1749-1761.

Wassef W (2016). Proposed guide specifications for wind loads on bridges during construction. *AASHTO SCOBS T5 Meeting*, Minneapolis, Minnesota, AECOM.

Yu M, Liao H, Li M, Ma C, Luo N, Liu M (2011). Study on static wind loading coefficients of suspension bridge, based on CFD simulation and wind tunnel test. *Applied Mechanics and Materials*, Switzerland, 66-68, 334-339.

Challenge Journal of Structural Mechanics

Research Article

Structural evaluation of unitized curtain wall systems by using inter-story drift test

Selcuk Dogru [a], Ferit Cakir [b,*], Bulent Akbas [b]

[a] *Erbay Aluminium Cons. Ind. & Trade Inc., Dilovası, 41455 Kocaeli, Turkey*
[b] *Department of Civil Engineering, Gebze Technical University, Gebze, 41400 Kocaeli, Turkey*

ABSTRACT

A curtain wall enhances the aesthetic appeal of a building and protects it from harmful environmental conditions. As one of the most significant façade curtain walls, Unitized Curtain Wall Systems (UCWS) are constructed concurrently with the construction of the structural framing system. Because of their lightness, ease of application, functionality, and various design possibilities, UCWSs are frequently used as exterior panels on high-rise buildings. UCWSs must be designed to resist external loads such as wind and seismic load during their lifetime. A structural performance evaluation of the UCWSs is therefore one of the most important criteria for their design. American Architectural Manufacturers Association (AAMA) suggests conducting a full-scale test on a mock-up to determine the structural performance in accordance with AAMA 501.4. In this study, an inter-story drift test was performed according to the AAMA 501.4 standard on a two-story UCWS system, comprised of six panels 1430.8 mm wide and 4215 mm high. The structural behavior of the system was assessed using horizontal and vertical displacement meters that were placed at various points in the system. In addition, a simplified numerical model of the system was prepared and experimental studies were supported by finite element analysis.

ARTICLE INFO

Article history:
Received 29 December 2021
Revised 24 January 2022
Accepted 12 February 2022

Keywords:
Unitized curtain wall systems
Inter-story drift test
Structural performance assessment
Full-scale mock-up test
Finite element analysis

1. Introduction

Curtain walls are popular cladding systems that are used to enhance the aesthetic appeal of building structures and provide a barrier against harmful environmental factors. They are designed to support only their own weight, and they are not intended to make up a structural component of a building. Due to the non-structural nature of curtain walls, lighter and cheaper materials like glass and aluminum tend to be used to build them, helping to reduce construction costs. There are two general categories of curtain wall systems that can be identified today: the stick curtain wall system (SCWS) and the unitized curtain wall system (UCWS). The SCWS is a system of panels that are mainly installed on-site with mullions and transoms through which the expanse of glass, metal panels, and brise-soleil panels are seamlessly linked piece by piece (Fig. 1). In general, each mullion is supported by the slabs or beams that run along its perimeter. On the other hand, in a UCWS, the curtain wall is constructed of large components that are assembled in a factory, shipped to the site, and installed there. For the mainframe, aluminum profiles which usually stand one story high and are made of light aluminum are used. During the building process, opening vents, glazing, and infill panels are built into the units before they are transported to the construction site. Like in SCWSs, each unit in UCWSs is usually supported by the perimeter slabs and beams. Although vertical mullions elements and horizontal transoms elements surround glass or opaque panels in both systems, at present, the UCWSs with high-quality vertical closures are the most popular for curtain walls on high-rise and large buildings in general (Abdullah and Ronnett 2010). UCWS is generally produced as a single unit consisting of framing system with infill panel in a factory and installed as a single unit on construction site (Fig. 2) while SCWS is gen-

* *Corresponding author*. Tel.: +90-262-605-1000 ; Fax: +90-262-653-8490 ; E-mail address: cakirf@gtu.edu.tr (F. Cakir)
ISSN: 2149-8024 / DOI: https://doi.org/10.20528/cjsmec.2022.01.003

erally produced as separated framing system and glass infill. Therefore, SCWS systems consist of two stages, first of all, the installation of the frame system in the construction site, and then the assembly of the panels on this system. The two-stage setup takes longer and is more complicated than UCWS. In addition, since UCWS systems are produced with a standard production system in a factory, the margin of error is less than SCWS systems.

Fig. 1. Stick curtain wall system (SCWS) (Web-1, 2022).

Fig. 2. Unitized curtain wall system (UCWS) (Web-2 2022).

UCWSs of today, although they are considered quite simple, are generally sophisticated products. Therefore, UCWS design guidelines are available from several organizations, such as the European Committee for Standardization (EN 13830), ASTM International Standard (ASTM E1300) and American Architectural Manufacturers Association (AAMA 501.4). These standards have become widely used for guiding in many countries. Furthermore, there have also been numerous scientific studies conducted to evaluate the performance of these systems, as well as the design requirements. As an example, Lee et al. (2021) developed the curtain wall module system and the fastener elements to accommodate displacements and vibrations caused by dynamic seismic waves. Aiello et al. (2018) investigated the seismic loading behavior of curtain walls in order to contribute to improvements in designing and manufacturing seismic-resilient products. Lee et al. (2017) described how the optimal shapes for a building's curtain wall extrusions can be generated by using a parametrically controlled geometric model and a genetic algorithm. Doebbel (2016) proposed a concept to evaluate the effects of forces and displacements imposed on structural joints as a result of earthquakes occurring on UCWSs. Ilter et al. (2015) compared the structural and infiltration performance of the two identically detailed and manufactured prototypes of a UCWS following the EN 13830 and AAMA 501.4 Standards. Nardini and Al-Hammad et al. (2014) described a systematic approach for the evaluation and selection of curtain wall systems for the construction of medium-high-rise buildings.

In the literature, there have been some studies on UCWSs, but detailed studies on the structural performance evaluation of these systems are scarce. Thus, the purpose of this study was to conduct an inter-story drift test on a full-scale mockup in accordance with the AAMA 501.4 and to evaluate its performance using a finite element analysis based on the results of the inter-story drift test.

A mock-up test is usually preferred to ensure that a curtain wall system can be constructed, integrates correctly, and meets performance requirements. In a properly conducted mock-up test, designers can collaboratively resolve detail and compatibility issues that may arise during construction, verify the functionality of the proposed construction, and apply the results from the tests to the project to avoid expensive, repeated defects. UCWS designs that contain many small details and connections need mock-up tests to ensure they are functioning properly. Therefore, in the first stage of the study, a full-scale mock-up test was performed on a two-stories UCWS model consisting of six panels according to the standard testing protocol outlined in the AAMA 501.4 (Fig. 3). The experimental study was carried out at the Façade Testing Institute in Istanbul using a large test rig. The tests were conducted on a 1:1 scale model of the UCWS model, which had the same characteristics as the real product. As shown in Fig. 3, the test specimens consist of two identically detailed the UCWSs having 1430.8 mm wide by 4215.4 mm high. The systems were constructed of aluminum framing members and insulating glass panels. In this study, the UCWSs were evaluated for their performance when subjected to specified horizontal displacements akin to earthquakes. During the mock-up test, 18 Linear Variable Differential Transformers (LVDTs) were used, and all displacements were instantly recorded (Fig. 4).

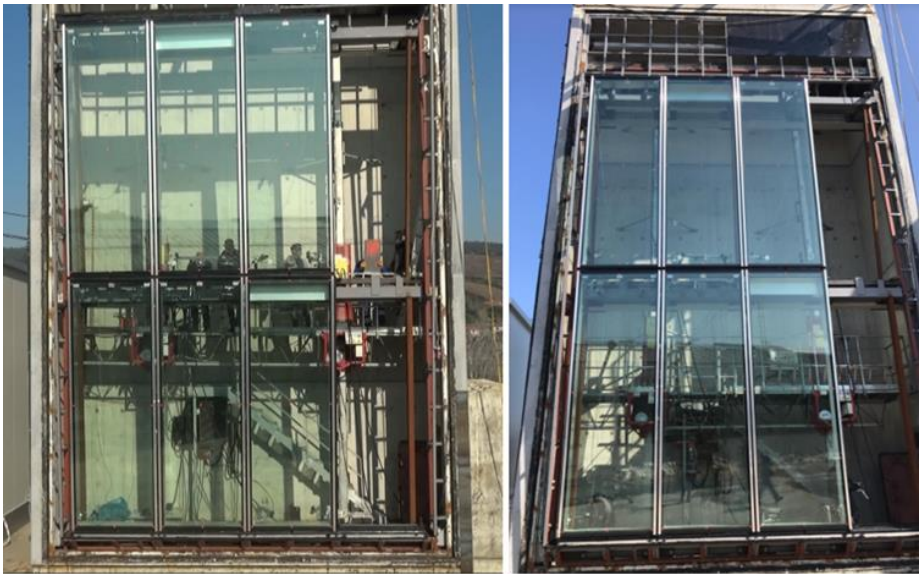

Fig. 3. Full-scale mock-up test.

Fig. 4. Linear variable differential transformers (LVDTs).

AAMA 501.4 defines an inter-story drift test for multi-story mock-ups as a measurement of relative horizontal movements between adjacent stories of a multi-story building. For this reason, a full-scale mock-up was tested for drift across stories in accordance with AAMA 501.4. For inter-story drift tests, the drift amount must equal 0.01 times the story height. Thus, the UCSW system was pushed in 11 steps from the inter-story section, and a total horizontal translation of 44 mm was applied at the end of the test. Fig. 5 displays the thrust point and LVDT numbers at the measurement points. In Table 1 and Fig. 6, the lateral translations of the LVDTs are presented based on the full-scale mock-up test.

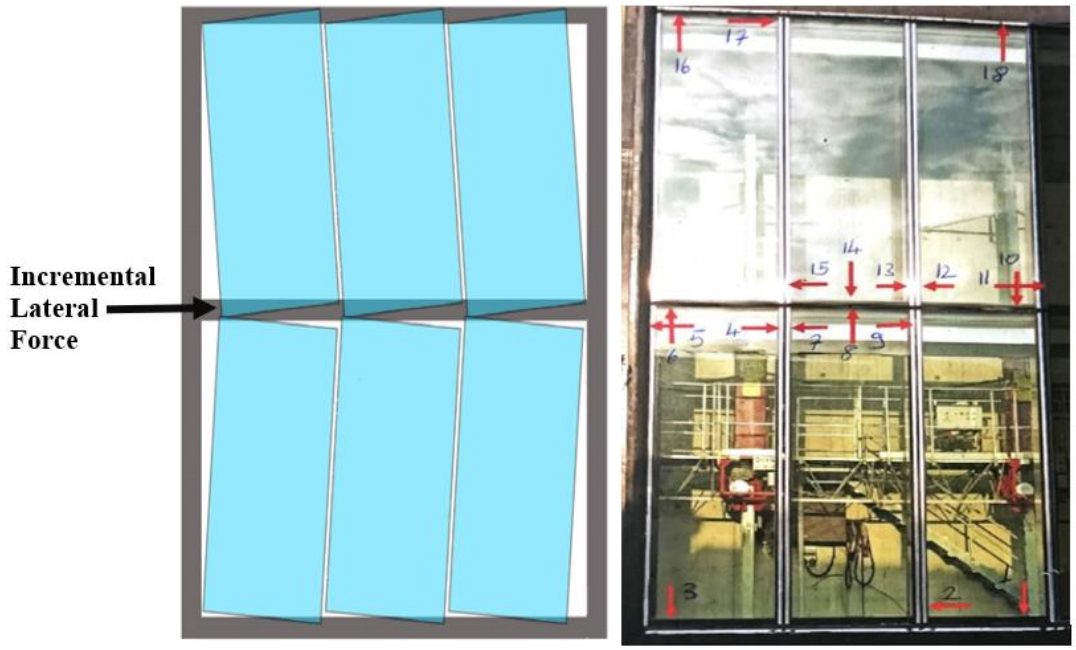

Fig. 5. The inter-story drift test and the LVDT IDs.

Table 1. Full-scale mock-up test results.

LVDT ID	Loading Steps										
	Step-1	Step-2	Step-3	Step-4	Step-5	Step-6	Step-7	Step-8	Step-9	Step-10	Step-11
1	-0,56	-0,91	-1,08	-1,32	-1,38	-1,36	-1,32	-1,37	-1,39	-1,43	-1,55
2	0,35	0,70	0,89	1,20	1,48	1,62	1,73	1,90	2,08	2,28	2,45
3	0,13	0,33	0,50	0,66	0,88	1,04	1,25	1,38	1,54	1,73	1,98
4	-4,04	-7,67	-10,65	-14,57	-18,85	-22,37	-26,01	-30,10	-33,82	-37,59	-41,34
5	4,12	7,84	10,89	14,78	19,19	22,79	26,57	30,61	34,37	38,22	41,88
6	-0,10	-0,31	-0,47	-0,66	-0,84	-1,00	-1,18	-1,31	-1,46	-1,66	-1,90
7	-4,02	-7,72	-10,62	-14,54	-18,92	-22,45	-26,09	-30,26	-33,96	-37,80	-41,58
8	0,00	-0,17	-0,31	-0,52	-0,90	-1,25	-1,79	-2,19	-2,68	-3,18	-3,67
9	3,83	7,54	10,61	14,55	18,85	22,46	26,20	30,28	33,93	37,41	37,41
10	0,28	1,09	1,81	3,16	4,66	5,90	7,28	8,34	9,49	10,65	11,82
11	-3,36	-6,50	-9,36	-13,41	-17,82	-21,50	-25,24	-29,06	-32,58	-36,41	-40,35
12	3,31	6,43	9,09	12,93	17,26	21,01	24,82	28,81	32,47	34,97	34,97
13	-3,67	-6,82	-9,32	-12,55	-16,26	-19,57	-23,14	-27,20	-30,89	-34,75	-38,58
14	0,00	0,03	0,09	0,33	0,89	1,38	2,19	2,84	3,42	4,19	4,93
15	3,64	6,76	9,23	12,48	16,21	19,50	23,04	27,11	30,75	34,61	38,43
16	0,11	0,01	-0,09	-0,18	-0,35	-0,42	-0,57	-0,71	-0,87	-1,06	-1,41
17	-0,65	-0,98	-1,25	-1,56	-1,85	-2,11	-2,27	-2,61	-2,81	-2,98	-3,17
18	-0,29	-0,89	-1,62	-2,71	-4,01	-5,13	-6,30	-7,45	-8,58	-9,73	-10,87

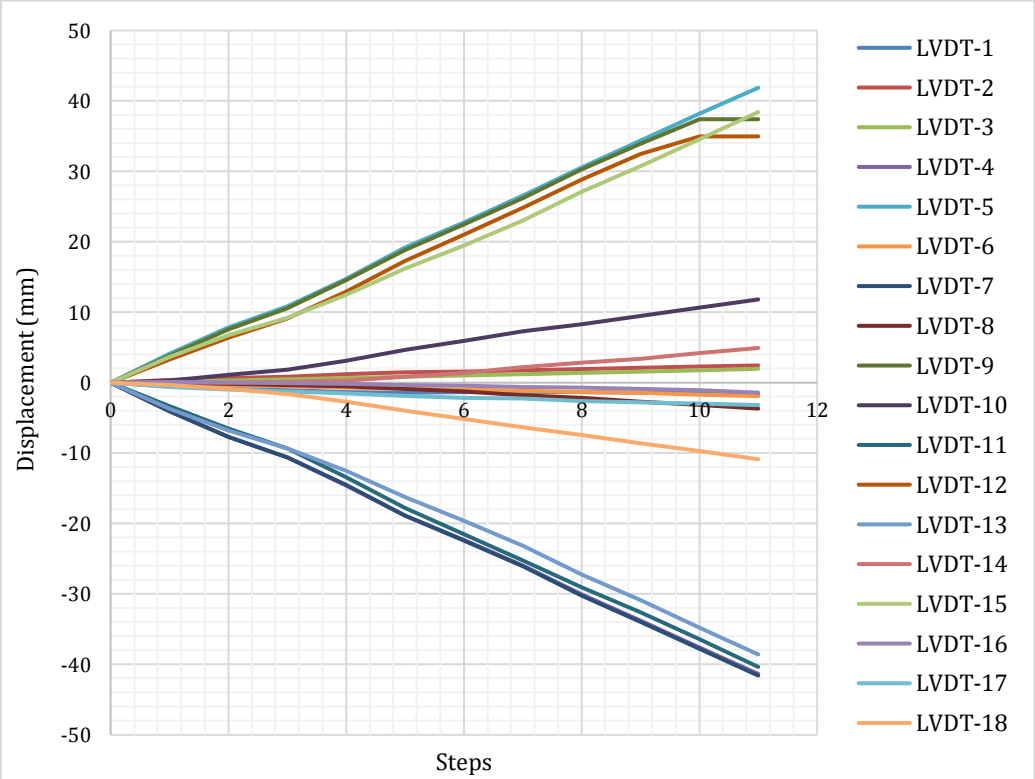

Fig. 6. Displacement records of the LVDTs.

2. Numerical Analysis

2.1. Finite element modeling (FEM)

As part of the second part of the study, the FEM for the inter-story drift test was developed and the finite element analysis was performed according to the loading protocol used to perform the mock-up test. The ANSYS Workbench program was used to build a FEM of the UCWS and some geometric features in the system were simplified while computing the finite element model. In the first stage of the finite element modeling studies, the entire experimental system was modeled in detail (Fig. 7). A simplification study was then conducted in order to reduce the analysis time of the model by reducing the number of parameters within it (Fig. 8). In the FEM, the simplified model was prepared using 1581533 nodes and 831560 elements (Fig. 9). Based on the operating principle of the system, the bottom and top parts of the panels are defined as fixed to translation and free to rotate as boundary conditions.

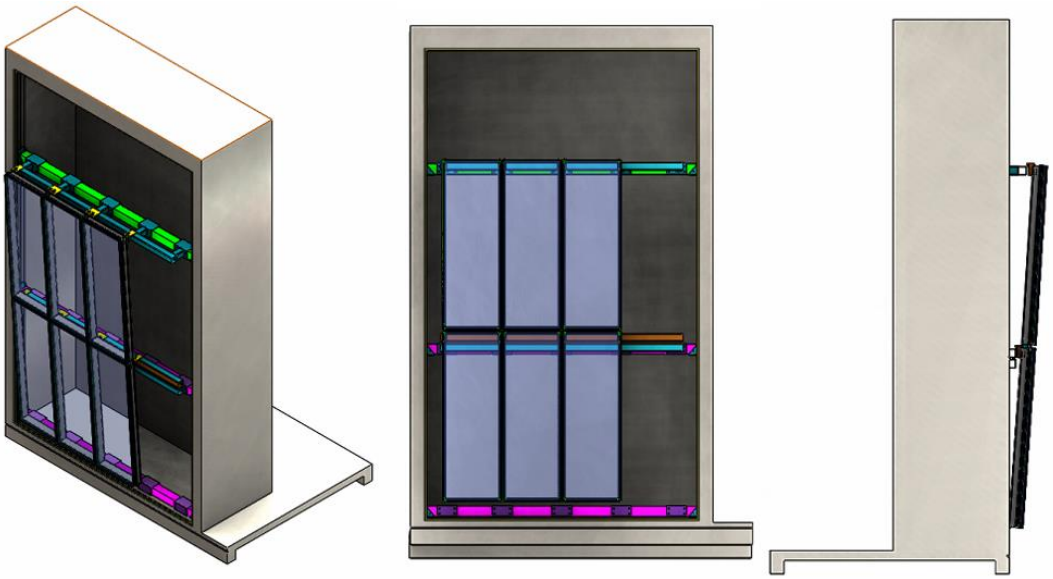

Fig. 7. Detailed 3D model of the experimental setup.

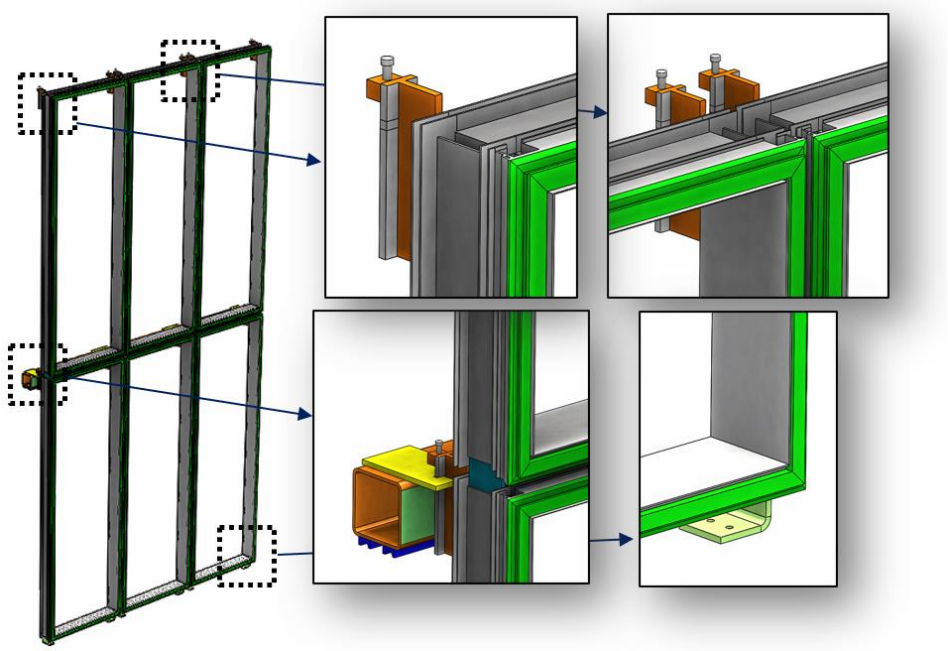

Fig. 8. Simplified 3D model of the experimental setup.

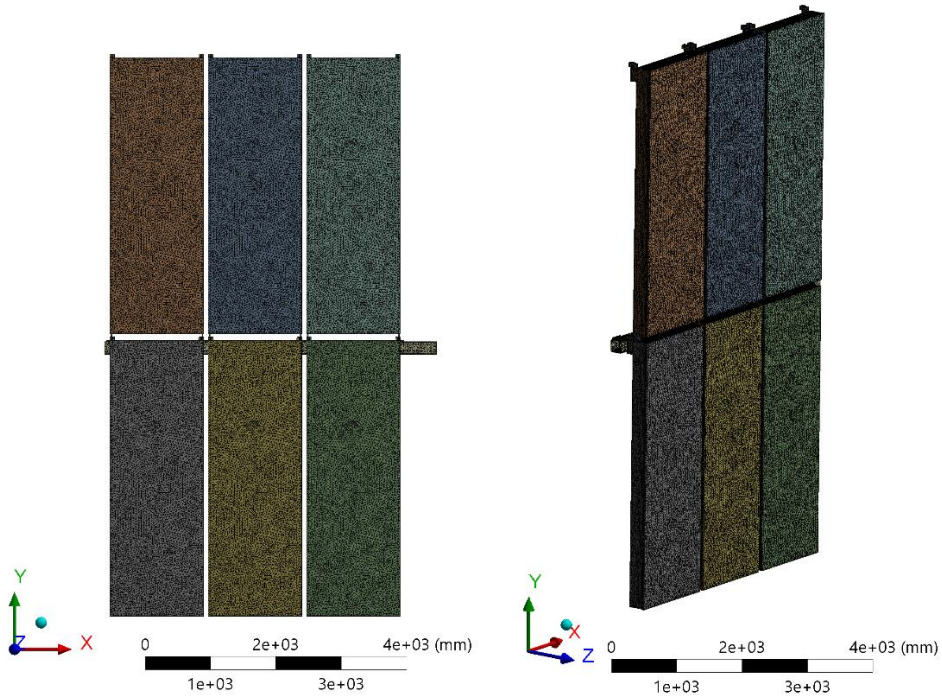

Fig. 9. Simplified finite element model.

2.2. Finite element analysis (FEA)

In this study, the structural components of the UCWS were designed as structural steel, aluminum and glass by considering the experimental system and the properties of the materials obtained from the ANSYS library are summarized in Table 2.

In the FEA, the FEM was applied to 44 mm of lateral displacement over 11 steps based on the experimental results (Fig. 10). At the LVDTs located points, the lateral and vertical displacements were recorded at each step in the FEA. Then, the experimental test and numerical results were compared and checked for compatibility. Relations between the FEA and test results are graphically shown in Fig. 11.

According to the comparisons, it can be concluded that a similar pattern emerged between the experimental and numerical data. Moreover, the FEA results had well symmetry in vertical and lateral displacements. When both the experimental and FEA results were examined, it was seen that the general trend is a linear translation behavior. However, for the LVDT-8 and LVDT-14, the FEA results were a little different from the experimental results. This may be caused by errors in the experimental data or by perfect conditions in the FEM (Fig. 11).

Table 2. Mechanical properties of the structural components.

	Young's Modulus (Pa)	Poisson's Ratio	Density (kg/m3)
Steel	2E+11	0.30	7850
Aluminum	7.1E+10	0.33	2770
Glass	7.2E+10	0.20	2500

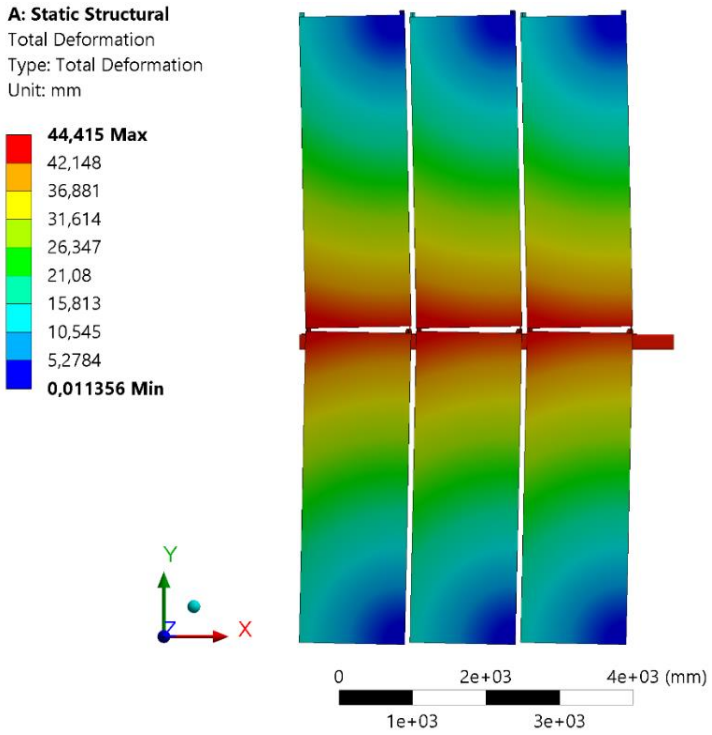

Fig. 10. Total deformation of the system.

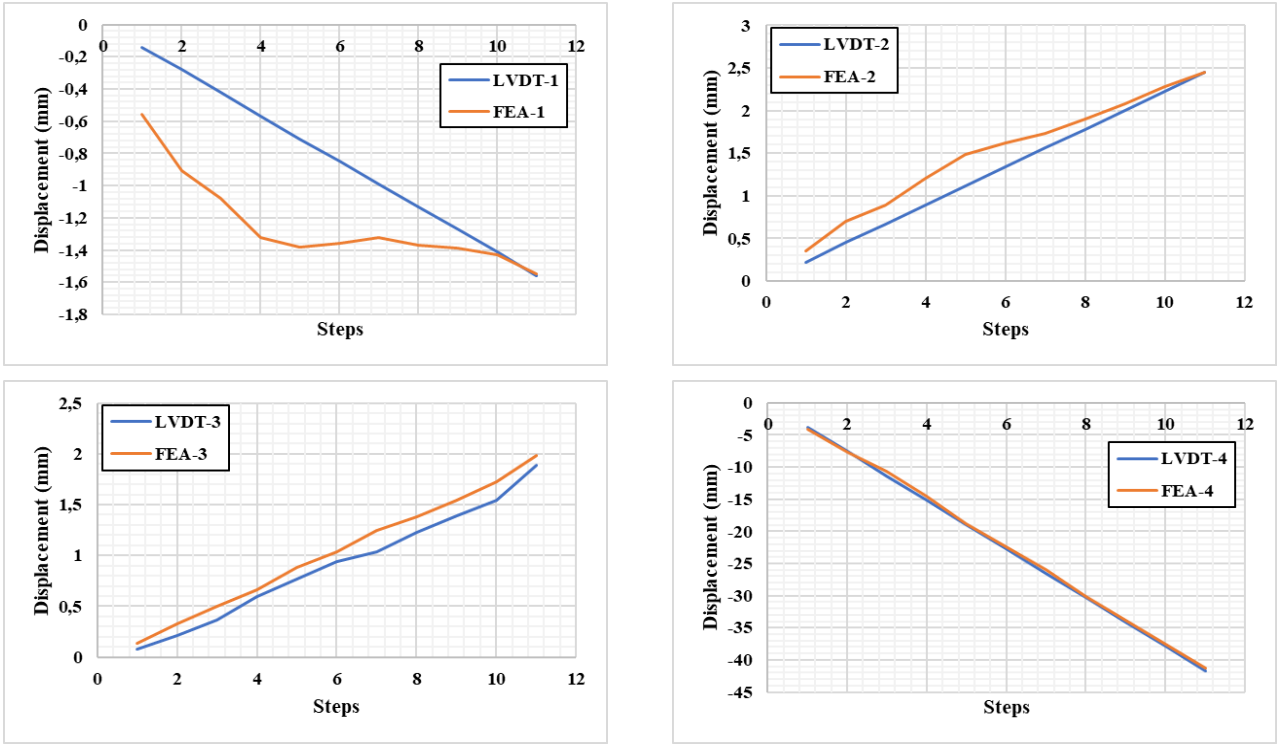

Fig. 11. (continued)

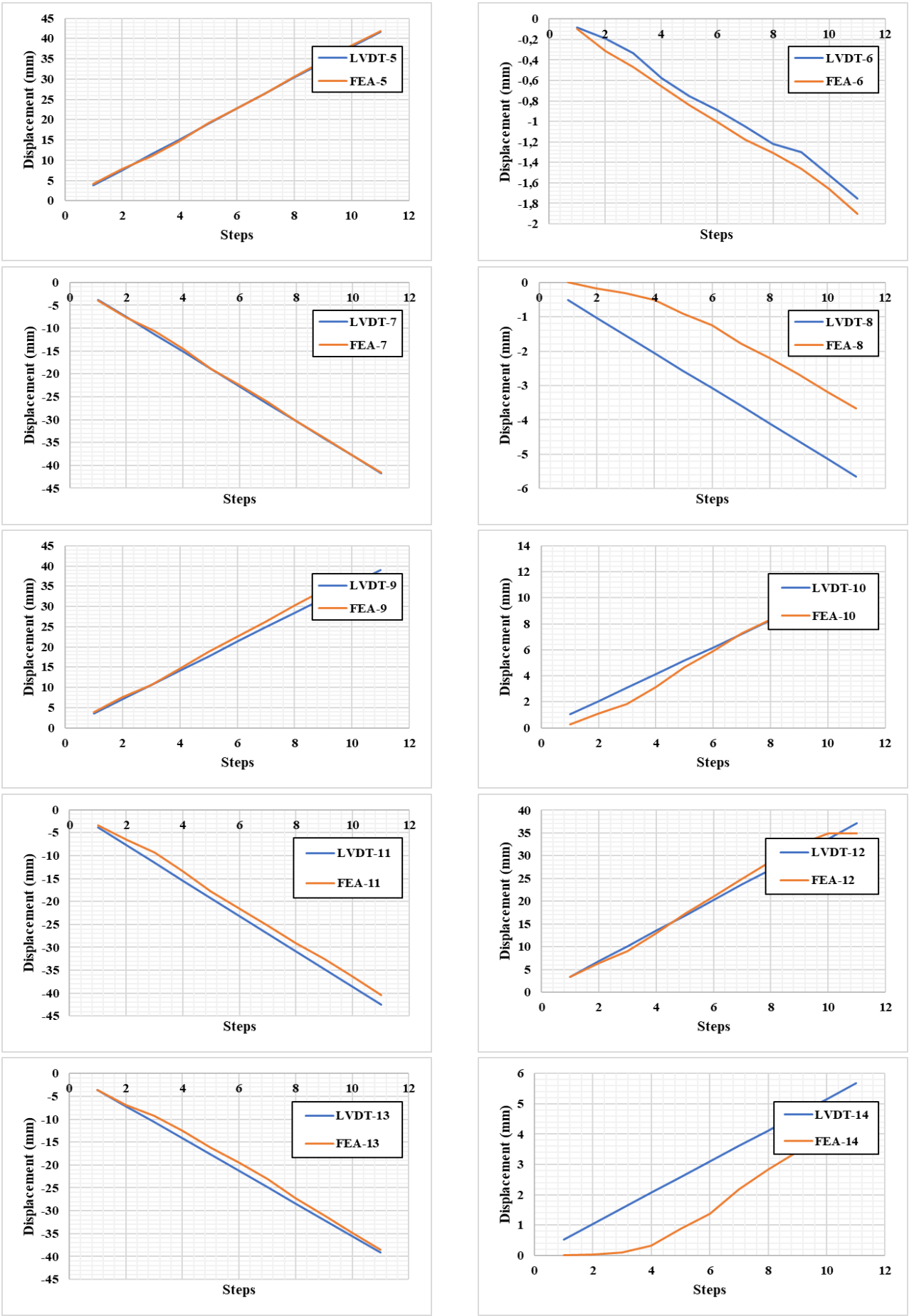

Fig. 11. (continued)

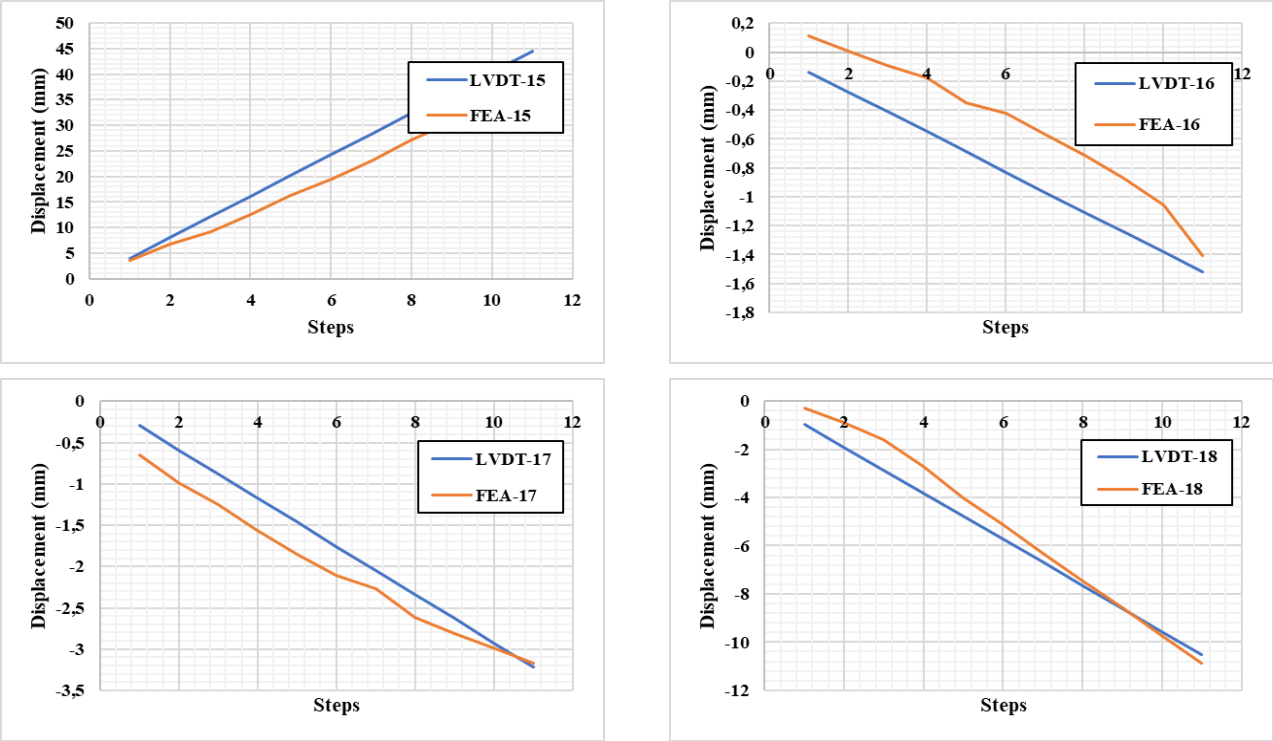

Fig. 11. Comparisons of displacement between experiments and FEA model.

3. Conclusions

The curtain walls of many buildings enhance their aesthetic appeal and protect them from damaging environmental conditions. Unitized curtain wall systems (UCWS) are one of the most significant curtain walls because they can be manufactured concurrently with structural framing. Because of their superior characteristics such as their lightness, ease of installation, and functionality, they are widely used to cover the exteriors of high-rise buildings. The objective of this study is to conduct a full-scale mockup test according to AAMA 501.4 and evaluate its performance based on the results of the inter-story drift test. A large test rig is used as part of the experiment at the Façade Testing Institute in Istanbul. The tests are conducted on a 1:1 scale model of the UCWS, which has the same features as the real product. The UCWS is pushed in a total of 11 steps from the inter-story section and is translated horizontally by 44 mm, which is equal to 0.1 times the story height. During the mock-up test, all displacements are recorded instantly with 18 LVDTs. A simplified numerical model of the system is also prepared to support the experimental studies.

Based on the results obtained from the investigation, it is observed that the wall system was successful according to the AAMA 501.4. Moreover, the data from the LVDTs indicates that the panels exhibit linear behavior, while the system exhibits rigid diaphragm behavior. A similar pattern can be seen in the finite element analysis. It is convenient to see that the records taken from the LVDTs and the records taken from the finite element model are very similar. These results demonstrate that simplification processes are facilitated the numerical modeling of the complex curtain wall systems. It is expected that the results gotten from this research will become the basis for further research into the same issue. In addition. The dynamic behaviour of the UCWSs should be further investigate through the cyclic loading history.

Publication Note

This research has previously been presented during the 6th International Conference on Earthquake Engineering and Seismology (6ICEES) held in Gebze Technical University, Turkey, on October 13-15, 2021. Extended version of the research has been submitted to Challenge Journal of Structural Mechanics and has been peer-reviewed prior to the publication.

Acknowledgements

The authors would like to thank Erbay Aluminium Company for its assistance in the experimental studies.

Funding

The authors received no financial support for the research, authorship, and/or publication of this manuscript.

Conflict of Interest

The authors declared no potential conflicts of interest with respect to the research, authorship, and/or publication of this manuscript.

REFERENCES

AAMA 501.4:00 (2000). Recommended Static Testing Method for Evaluating Curtain Wall and Storefront Systems Subjected to Seismic and Wind Induced Interstory Drift, The American Architectural Manufacturers Association (AAMA), USA.

Abdullah A, Ronnett M (2010). Exploration of Curtain Wall Solutions. *Perkins+Will Research Journal*, 2010(2), 33-55.

Aiello C, Caterino N, Maddaloni G, Bonati A, Franco A, Occhiuzzi A (2018). Experimental and numerical investigation of cyclic response of a glass curtain wall for seismic performance assessment. *Construction and Building Materials*, 187, 596-609.

Al-Hammad AM, Hassanain MA, Juaim MN (2014). Evaluation and selection of curtain wall systems for medium-high rise building construction. *Structural Survey*, 32(4), 299-314.

ANSYS Workbench (2020). Finite Element Software. Ansys Inc., Canonsburg, PA, USA.

ASTM E1300:16 (2016). Standard Practice for Determining Load Resistance of Glass in Buildings, American Society for Testing and Materials (ASTM), USA.

EN 13830:2015+A1 (2020). Curtain walling - Product standard. The European Committee for Standardization, Belgium.

Ilter E, Tavil A, Celik OC (2015). Full-scale performance testing and evaluation of unitized curtain walls. *Journal of Facade Design and Engineering*, 3(1), 39-47.

Lee H, Oh M, Seo J, Kim W (2021). Seismic and energy performance evaluation of large-scale curtain walls subjected to displacement control fasteners. *Applied Sciences*, 11(15), 6725.

Nardini V, Doebbel F (2016). Performance-based concept for design of structural silicone joints in façades exposed to earthquake. *Challenging Glass Conference Proceedings*, 5, 283-294.

Web-1 (2022). https://openlab.citytech.cuny.edu/building-newyork/2017/11/08/stick-system-curtain-wall-installation/ (Access Date: 04.02.2022)

Web-2 (2022). https://www.mornglass.com/wp-content/uploads/2021/05/unitized-curtain-wall-installation-insulated-glass-morn-bm.jpg (Access Date: 04.02.2022)

Challenge Journal of Structural Mechanics

Research Article

Earthquake resistant design of reinforced concrete retaining walls considering the project location change effect

Zülal Akbay Arama [a], İlknur Dalyan [b,*], Muhammed Selahaddin Akın [c]

[a] *Department of Civil Engineering, İstanbul University-Cerrahpaşa, 34320 İstanbul, Turkey*
[b] *Department of Civil Engineering, Çanakkale Onsekiz Mart University, 17020 Çanakkale, Turkey*
[c] *Kartal Municipality, 34862 İstanbul, Turkey*

ABSTRACT

In this paper, the design process of reinforced concrete retaining walls is investigated under the issue of "project location change effect" which becomes a significant requirement to assess the earthquake resistant design depending on the new Turkish Building Earthquake Code-2018 (TBEC-2018). Within this context, in the light of the related code, fourteen different districts which are located in the Anatolian Side of Istanbul Province (Turkey) have been taken into consideration, to search for also the effects of the supported earth fill depth, the unit weight and the shear strength angle of surrounding soil and the external loading conditions. In this way, it has been aimed to focus on the application details of the design code and reflect the outcomes of the analysis in terms of the changes that happened in wall dimensions depending on the locations of project. Besides, with this study, it is aimed to reveal that the definition of type sectional wall will not be possible with the new code. As the result, the influence rates of the investigated project variants have been explained considering site-specific retaining wall design in terms of integrated relations of the design parameters.

ARTICLE INFO

Article history:
Received 7 February 2022
Revised 1 March 2022
Accepted 16 March 2022

Keywords:
Retaining walls
Location effect
Sizing
Turkish Building Earthquake Code

1. Introduction

The earthquake-resistant design of reinforced concrete retaining walls has been the main subject of several studies till now depending on the widespread usage and easily applicable characteristics of the retaining walls.öThe design of retaining walls is based on both the attainment of the geotechnical stability in terms of sliding, overturning and bearing capacity adequateness and the fulfilment of the structural requirements based on the envisaged codes to resist static and dynamic loads. In this context, Ahmadi-Nedushan and Varaee (2009) performed analyses for the optimal design of RWs with the Particle Swarm Optimization method to minimize both cost and weight. Kaveh and Khayatazad (2014) utilized the Ray optimization method to optimize RWs and check the design parameters with the determination of seismic active earth pressure with the pseudo-dynamic method. Uray et al. (2019) used the discrete optimization method with the use of the minimum weight of the wall as the objective function and formed a brief parametric study depending on only static conditions. Konstandakopoulou et al. (2020) conducted analyses for the design of RWs under static and seismic conditions with the satisfaction of all structural and geotechnical necessities according to European Code requirements with optimization algorithms during the decrement process of the ultimate cost. Dagdeviren and Kaymak (2020) derived a new regression model through the use of the Artificial Bee Colony algorithm to ensure the pre-design of RWs that is resting on the soil layer which has a high bearing capacity for static loading conditions. Besides, nowadays, there are various studies considering different methods and codes that are conducted to design RWs under static or/and dynamic conditions. The suggestions presented in the design codes or technical guidelines lead to the determination procedures of the lateral pressures (Kramer 1996). These codes and standards are

* *Corresponding author*. Tel.: +90-286-218-0018 ; E-mail address: ilknur.dalyan@comu.edu.tr (İ. Dalyan)
ISSN: 2149-8024 / DOI: https://doi.org/10.20528/cjsmec.2022.01.004

set up by considering earthquakes that have occurred or are likely to occur at relevant locations. Considering the destructive earthquakes that happened in Turkey like Erzincan-1992 (6.6 M_w), Adana-Yüreğir-1998 (6.2 M_w), Düzce-1999 (7.1 M_w), Gölcük-1999 (7.6 M_w), Bingöl-2003 (6.3 M_w), Van-2011 (7.1 M_w), Gökçeada-2014 (6.5 M_w), Elazığ-2020 (6.8 M_w) İzmir-2020 (6.6 M_w) the necessity to improve the existing code arose (AFAD). Therefore, a new Turkish Building Earthquake Code is developed in 2018 (TBEC-2018) depending on the prepared actual Earthquake Hazard Map of Turkey (TDTH 2018; Akkar et al. 2018).

In the context of this study, the consideration of the TBEC-2018 requirements for the design of reinforced concrete retaining walls to determine the earthquake effects have been made depending on the locations of immediate vicinities in the Anatolian side of Istanbul (Turkey). For this purpose, fourteen districts are taken into consideration and, also the effects of the change of excavation depth (supported earth fill depth), the unit weight of the surrounding soil, the shear strength angle of the surrounding soil and, the external loading magnitude has been searched. The coordinates of the city halls have been selected as the mentioned fourteen different locations. For this aim, macro codes are generated via Microsoft Excel software. As a result of the study, the significance degrees of the investigated variants have also been explained in terms of integrated relations of the design parameters in comparison with the mostly used pseudo-static approach.

2. Material and Method

In Fig. 1, the load distribution along a T-shaped retaining wall section generated depending on the earthquake condition has been given. Besides, the abbreviations that are used to describe the parts of the wall system is also given in the figure. B, z, H, d_{p1}, d_{p2}, t_1, t_2 represents the foundation base width, the supported earth fill depth, the total height of the wall, the thickness of the stem at the top, the thickness of the stem at bottom, the width of the wall toe and the width of the wall heel respectively.

In Fig. 1, the weight of the wall stem, the foundation base, the backfill soil is represented with W_w, W_{fb}, W_{sb} respectively and the surcharge is abbreviated by q_a. P_{as} and P_{ps} define the active and passive lateral soil forces respectively. P_{tb} is the base pressure and P_{qa} is generated force depending on the surcharge loading and P_{eqa} represents the active pressure due to the surcharge load for earthquake condition. In addition, the lateral soil pressures including both the active and passive states for earthquake condition are defined by P_{eas} and P_{eps} respectively.

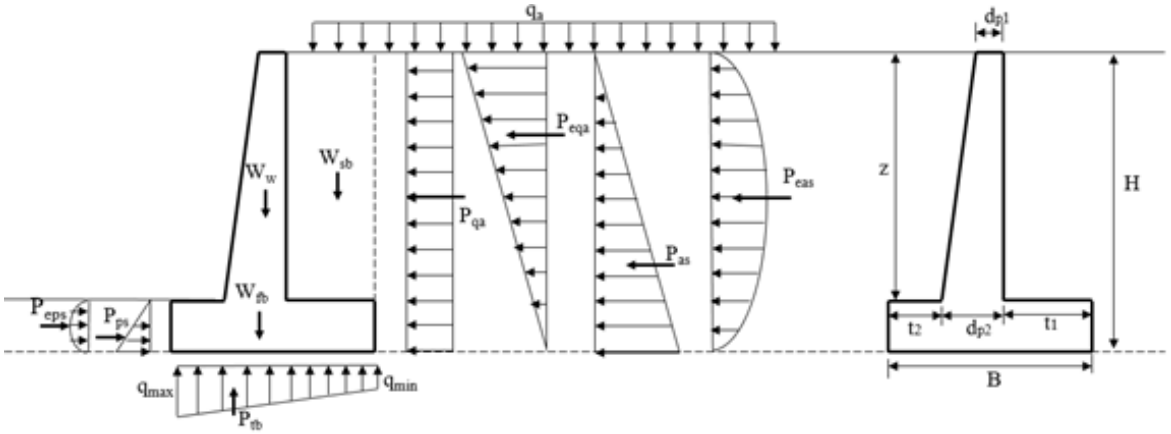

Fig. 1. The load distribution along the T-shaped retaining wall section.

In Fig. 2, the application details of TBEC-2018 are given to design RWs considering the remarkable effect of project location in terms of the geotechnical parameter determination process considering the dynamic response. The application process of TBEC-2018 begins with the identification of the class of the soil formation dominated in the project field. The code requires to obtain the accurate representative parameters of soil formation and in addition, necessitates to use the existing coordinates of the project field. The development of the new earthquake hazard map leads to discontinuing the concept of earthquake zone, and in the new map, unlike the previous map, instead of the earthquake zones, the peak ground acceleration (PGA) values are given. With the consideration of the earthquake active faults, it started to be entered into calculations as separate spectrum values and acceleration values for each location. In the context of this study, the seismic hazard maps in terms of peak ground acceleration, peak ground velocity, 5%-damped pseudo-spectral accelerations at 0.2 sec and 1.0 sec periods for return periods of 43, 72, 475 and 2475 years have been produced. In addition, the determination of the lateral earth coefficients is depended on the short period design spectral acceleration coefficient (S_{DS}) value. S_{DS} value varies according to each location on the map and soil classes that are defined in TBEC-2018. Besides, S_{DS} value can take five different values depending on the soil classes and these values can be acquired interactively from the earthquake hazard map. Therefore, lateral earth coefficient values vary according to each soil class defined in TBEC-2018. Within this context, Gürsoy (2013) articulated the necessity of the consideration of the soil parameters in the response spectrums for the safer designs with the discussion of the

previous earthquake design code of Turkey and Eurocode -8. Considering the requirements arising from the new earthquake code, Öztürk (2018) compared the last two codes used in Turkey in terms of the designs that are modelled for different locations within the same province. Keskin and Bozdoğan (2018) investigated the application details of the new code with the evaluation of another province, Kırklareli. Elçi and Göker (2018) discussed the last two design codes in terms of the design of reinforced concrete columns. Kayhan and Demir (2018) used a method based on the differential development algorithm technique in the design of reinforced concrete cantilever retaining walls at minimum cost. Özberk and Kahyaoğlu (2018) conducted the comparative analysis to see the effects of the change in wall height depending on the last two codes. Aksoylu et al. (2020) conducted a comparative analysis considering the design requirements of reinforced concrete buildings depending on the last two codes. Atmaca et al. (2019) were also compared to the last two codes considering a school project constructed in Gaziantep with the use of SAP2000 software. Yüksel and Akbaş (2020) determined the lateral soil pressures that are affecting a cantilever retaining wall depending on the last two earthquake design codes and investigated the surcharge loading effect on the dimensions.

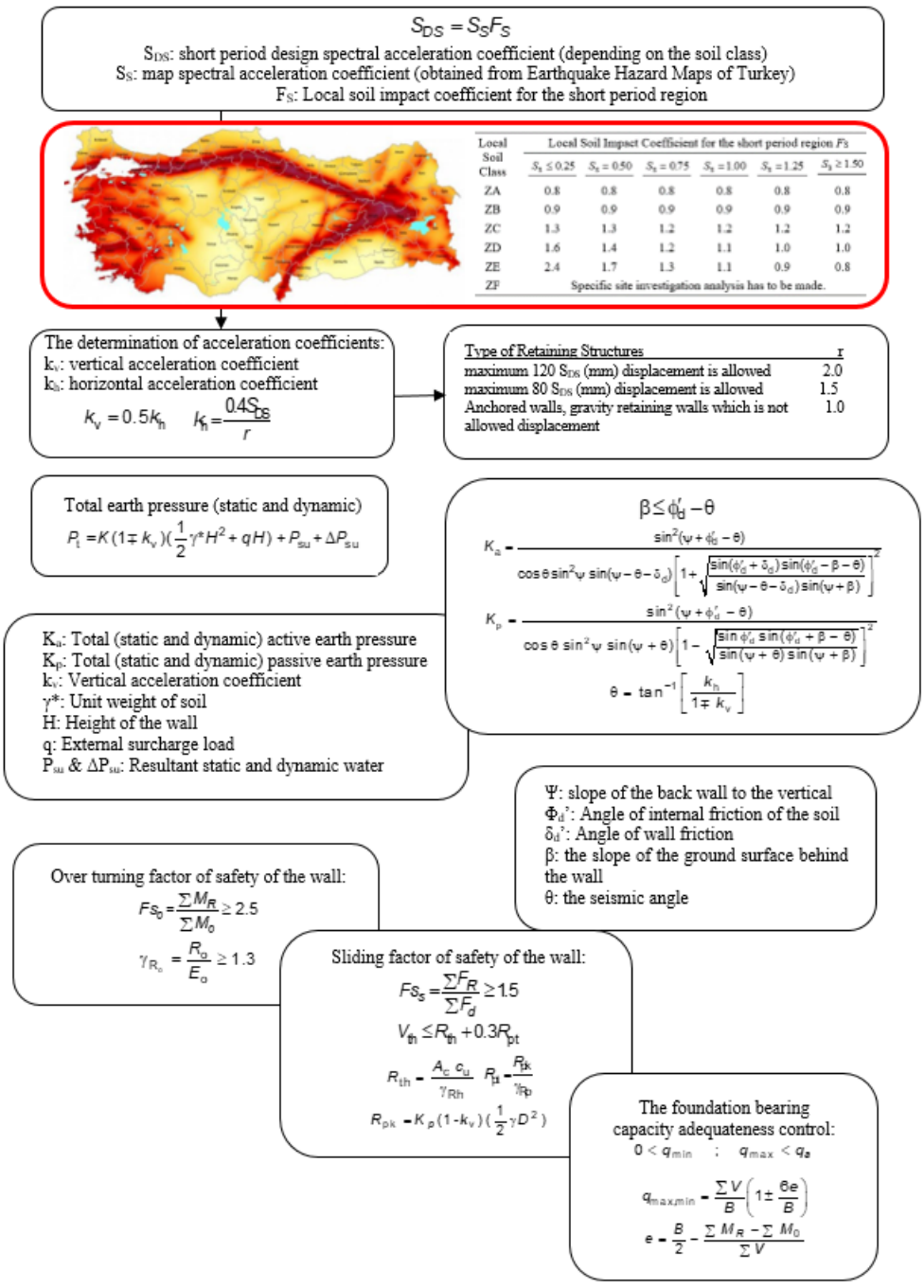

Fig. 2. The flowchart for designing RWs according to TBEC-2018.

3. Parametrical Analysis

Parametrical analyses were conducted according to the change of design parameters such as the supported earth fill depth, the unit weight and, the shear strength angle of the surrounding soil, the external loading conditions and, the location of the project site. In this context, the supported earth fill depth was assumed to be 3, 6, 9 m, the unit weight of the soil was selected as 17, 19, 21 kN/m^3, the shear strength angle of surrounding soil was 30, 31, 32, 33, 34°, the external load was 0 and 15 kPa. The soil class was assumed to be ZB for all the considered cases. Besides, the location effect was taken into consideration depending on the selected 14 different places in Istanbul Province from the Anatolian side. The location of European and Anatolian sides of Istanbul Province is shown in Fig. 3a and the selected districts are exhibited in Fig. 3b. These districts are Adalar, Ataşehir, Beykoz, Çekmeköy, Kadıköy, Kartal, Maltepe, Pendik, Sancaktepe, Şile, Sultanbeyli, Tuzla, Ümraniye, Üsküdar respectively.

The obtained values of S_S and S_{DS} from the Earthquake Hazard Map of Turkey depending on the locations of the districts are given in Table 1. The details of the attainment process of the PGA values that are used to determine the S_{DS} values can be ensured by the interactive web application of Earthquake Hazard Map of Turkey that is given in Fig. 4.

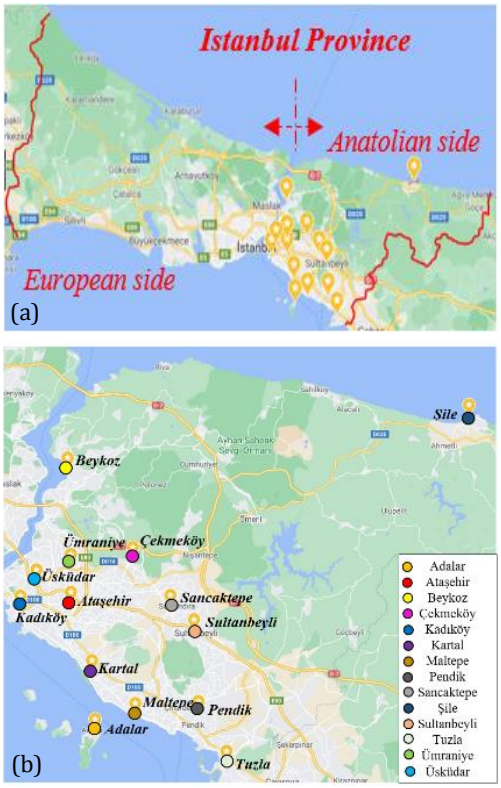

Fig. 3. (a) Map of Istanbul Province; (b) Location of investigation location.

Table 1. The obtained values of S_S and S_{DS} from the Earthquake Hazard Map of Turkey depending on the coordinates of the districts.

No	District	X	Y	PGA (g)	SS	SDS
1	Adalar	40.87438701	29.13267396	0.523	1.276	1.148
2	Ataşehir	40.98375666	29.11600874	0.379	0.890	0.801
3	Beykoz	41.12695186	29.09775237	0.278	0.665	0.599
4	Çekmeköy	41.03323219	29.16828953	0.323	0.762	0.686
5	Kadıköy	40.99326509	29.03723949	0.392	0.958	0.862
6	Kartal	40.89009159	29.18387493	0.458	1.116	1.004
7	Maltepe	40.93144641	29.12791484	0.441	1.069	0.962
8	Pendik	40.87663041	29.23256815	0.447	1.034	0.931
9	Sancaktepe	40.99412562	29.23041597	0.340	0.816	0.734
10	Şile	41.17749167	29.61098592	0.245	0.583	0.525
11	Sultanbeyli	40.97081508	29.25938800	0.352	0.845	0.761
12	Tuzla	40.84360330	29.30085842	0.477	1.174	1.057
13	Ümraniye	41.02992824	29.09882910	0.339	0.821	0.739
14	Üsküdar	41.02066768	29.01974777	0.367	0.894	0.805

According to Table 1, if the achieved S_{DS} values are arranged in descending order, $S_{DS(\text{Adalar})} > S_{DS(\text{Tuzla})} > S_{DS(\text{Kartal})} > S_{DS(\text{Maltepe})} > S_{DS(\text{Pendik})} > S_{DS(\text{Kadıköy})} > S_{DS(\text{Üsküdar})} > S_{DS(\text{Ataşehir})} > S_{DS(\text{Sultanbeyli})} > S_{DS(\text{Ümraniye})} > S_{DS(\text{Sancaktepe})} > S_{DS(\text{Çekmeköy})} > S_{DS(\text{Beykoz})} > S_{DS(\text{Şile})}$ is obtained. Totally 1260 design analyses were performed with the use of TBEC-2018 to search for the effect of the location effect on the design in relation with other variants of the analyses.

4. Results and Discussion

In Fig. 5, the change of the wall foundation base width against shear strength angle is given depending on different districts. The unit weight of the surrounding soil is assumed to be 21 kN/m^3 to evaluate only the effects of shear strength angle change. In addition, Fig. 5a-c concerns the change of the excavation depth. The comparison

of Fig. 5a-c shows that the increase of the excavation depth leads the design to enlarge the base. The triple increase of the excavation depth causes to enlarge *B* approximately as triple times the value that is determined for 3-meter excavation depth. The main theme of this study is to investigate the location effect of the project site. Therefore, the individual evaluation of the figures gives the average approximations for design dimensioning depending on the change of the location. For 3-meter excavation depth at Φ=30°, the dimensions of the wall system were not affected by the change of the coordinate.

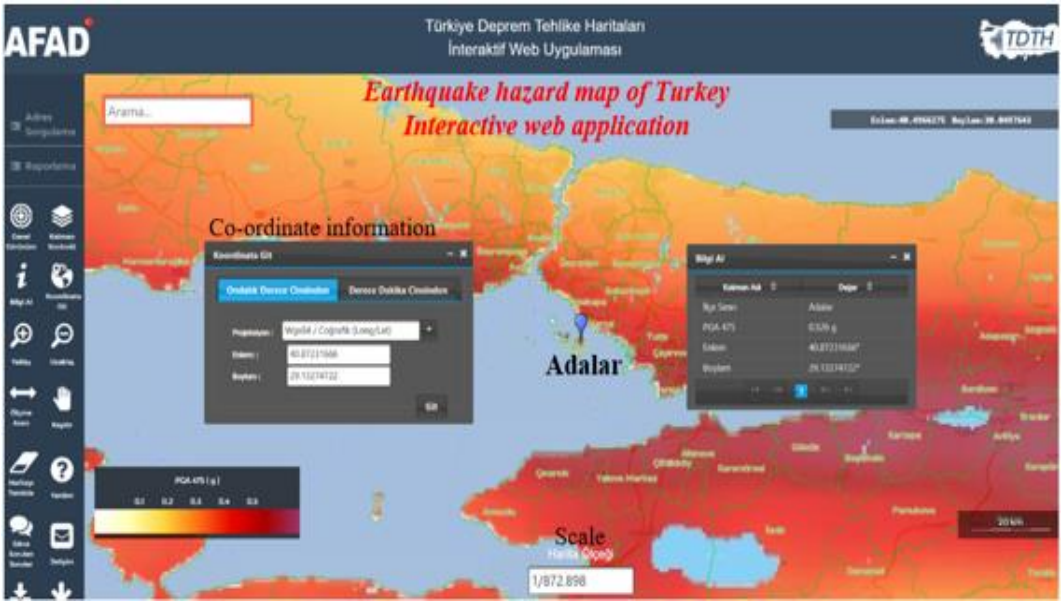

Fig. 4. The interactive web application of Turkey earthquake hazard map.

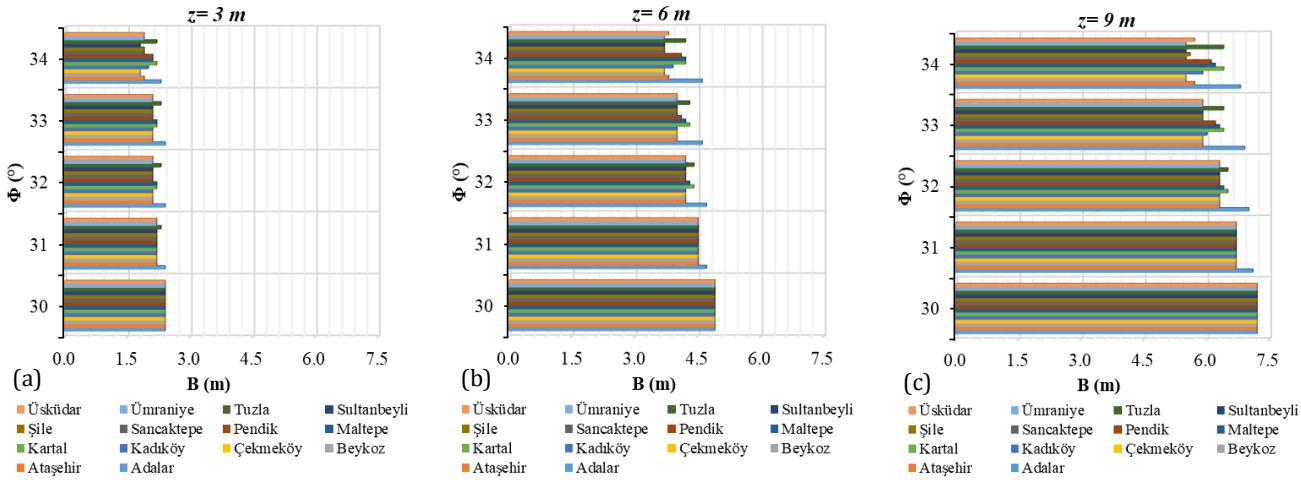

Fig. 5. The change of *B* against the shear strength angle:
(a) for *z*=3m situation; (b) for *z*=6m situation; (c) for *z*=9m situation.

This situation may be arisen because of the attainment of the limit design sizing due to the smallness of the soil strength. In other words, in such a case, the design may access the maximum dimension limits envisaged by the code depending on the suggested safety factors at earthquake condition. The increase of the friction angle ensures the surrounding soil to support the additional loads. Therefore, it is expected the designer to reduce the sizing of RW when the increase of the shear strength angle is possible. For all the foreseen excavation depths studied in the context of this study, the maximum dimensions were obtained for the case that minimum shear characteristics were used. Besides, B value possesses the biggest amount in Adalar district for all the defined different shear strength properties compared to other districts. Adalar district has the biggest value of S_{DS} (1.148) that is increasing the affected active total earth pressure value. It shows that the width *B* is directly proportional with the change of S_{DS} value. If a comparison is conducted between the determined maximum and minimum *B* values at different districts, at *z*=3 m, it is found that 28% increase of the width is necessary to support the same earth fill at 34° shear strength angle. This situation remarks that it is not possible to use a standard type sec-

tion proposed in the projecting of retaining walls. In such a case, the construction of the same wall section for every district leads to problematic constructions in terms of earthquake safety. Additively, the maximum change of the *B* width is happened in Çekmeköy, Beykoz and Sultanbeyli districts depending on the increase of the shear strength angle to 34° from 30°. In such a case the width is necessitated to decrease by approximately 33%. The minimum change of the *B* width is happened in the Adalar district depending on the increase of the shear strength angle to 34° from 30°. In such a case the width is necessitated to decrease by approximately 4.5%. The increase of the excavation depth to 6-meters leads to enlarging the base and the relative difference of the *B* that is happened between the envisaged maximum and minimum shear characteristics remains approximately 33%. At 6-meter excavation depth, the minimum change of the B has again happened in Adalar district but the decrease of the *B* is reached to 6% ratio depending on the increase of the shear strength angle to 34° from 30°.

The last evaluated excavation depth is 9-meters. In this situation, the maximum change of the *B* has happened with a decreasing tendency of approximately 33% again between the maximum and minimum shear characteristics. It means that, for example, retaining wall construction is fictionalized in the Beykoz district, if the surrounding soil shear properties of the wall is selected 30°, the width of the base will be 7.2-meters. But if the surrounding soil is preferred to be used more strengthen (Φ=34°) the width of the base will reduce to be 5.5-meters. Besides, the decrease of the *B* is determined 6% if the shear strength angle rises to 34° from 30° in Adalar.

Fig. 6 is given to emphasize the significant effect of the change in the supported earth fill depth. In this case, the unit weight of the surrounding soil is assumed to be 21 kN/m^3 and the shear strength angle is selected to be 34° depending on the obtained maximum change in *B* considering the districts. It can be clearly seen that considering the same soil conditions for surrounding soil the *B* value can be changed between 1.8 to 2.3 meters for 3 m depth, 3.7 to 4.6 for 6 m depth and 5.5 to 6.8 for 9 m depth of earth fill to support. This is the meaning that the *B* value can be differentiated approximately 25% (the value of the differentiation which is calculated as the mean value for all the considered earth fill depths) depending on the location independent from the soil conditions.

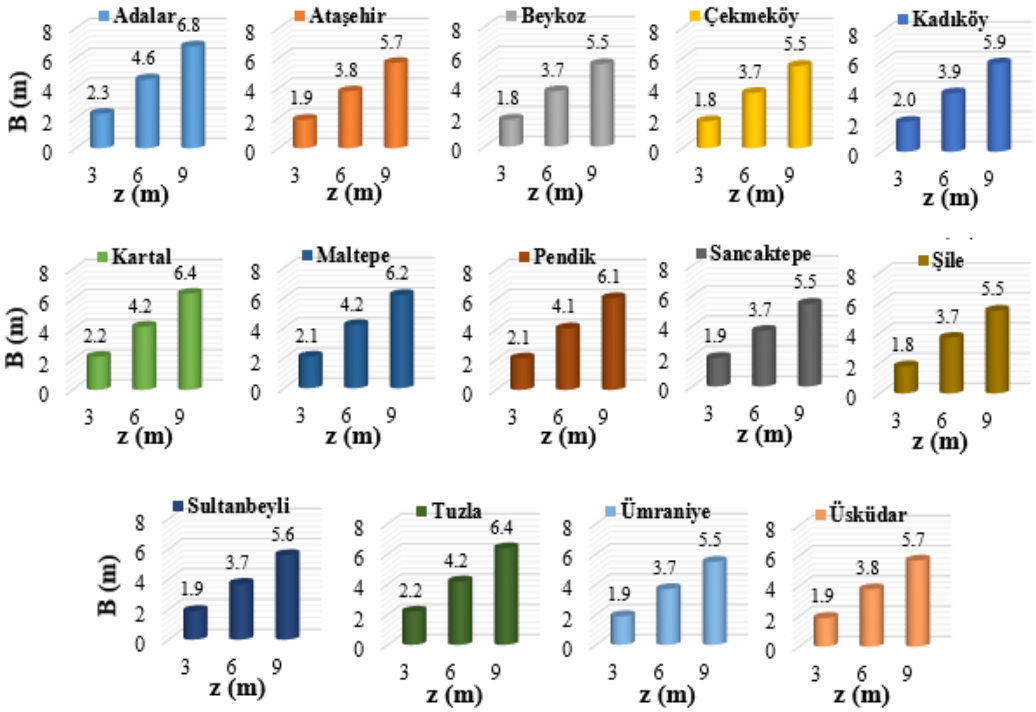

Fig. 6. The change of *B* against the excavation depth depending on the districts.

In addition, Fig. 7 is drawn to show the influence of the change of the soil unit weight depending on the supported earth fill depth which was assumed to be *z*=3m (Fig. 7a), *z*=6 m (Fig. 7b) and *z*=9 m (Fig. 7c) respectively. In this context, the unit weight of the surrounding soil was assumed to be 17 kN/m^3, 19 kN/m^3 and 21 kN/m^3 respectively. The shear strength angle of the surrounding soil was proposed to be constant at 32° to obtain only the effect of the change of soil unit weight. In Fig. 6, it is obviously clear that the effect of the change of soil unit weight has to be evaluated individually for the districts. In Fig. 6a, for *z*=3 m situation, the increase of soil unit weight has no effect on the *B* within Adalar district. For Tuzla, B increases nearly at the ratio of 4.3% if the soil unit weight is increased to 19 kN/m^3 from 17 kN/m^3, in addition, the increase of the soil unit weight to 21 kN/m^3 from 17 kN/m^3 increases the *B* width approximately 4.5%. The change of the *B* follows the same trend for Kartal, Maltepe and Pendik districts.

B is calculated 2.10 m, 2.20 m and 2.20 m for 17 kN/m^3, 19 kN/m^3, and 21 kN/m^3 respectively. This means that the use of a relatively dense material as the backfill, can be affect the B nearly 4.6%. Besides, *B* calculated for the designs in other districts have similar change characteristics. There happens an increase for the *B* approximately at the degree of 5% between the loosest and densest states of the surrounding soil strata.

In Fig. 7b, for *z*=6 m situation, *B* is determined 4.60, 4.65 and 4.70 m for 17 kN/m^3, 19 kN/m^3 and 21 kN/m^3 respectively in Adalar district. Differently from *z*=3 m situation, the deepen the excavation depth or the increase of the supported earth fill thickness has an integrated effect with the change of soil unit weight on dimensioning of the wall. The wall design considering the *B* change in Tuzla and Kartal districts exhibit the same path while the change of soil unit weight. In such a case, the *B* value is determined 4.30, 4.35 and 4.40 m respectively for 17 kN/m^3, 19 kN/m^3, 21 kN/m^3 respectively. For Maltepe district *B* is 4.20, 4.25 and 4.30 m and for Pendik district *B* is 4.10, 4.20 and 4.20 m in addition, the other districts have 4.00, 4.10 and 4.20 m of *B*, for the envisaged cases respectively. The acquired widths for *B* determination shows the increase rate of the effect of soil unit weight rises with the decrease of S_{DS} value.

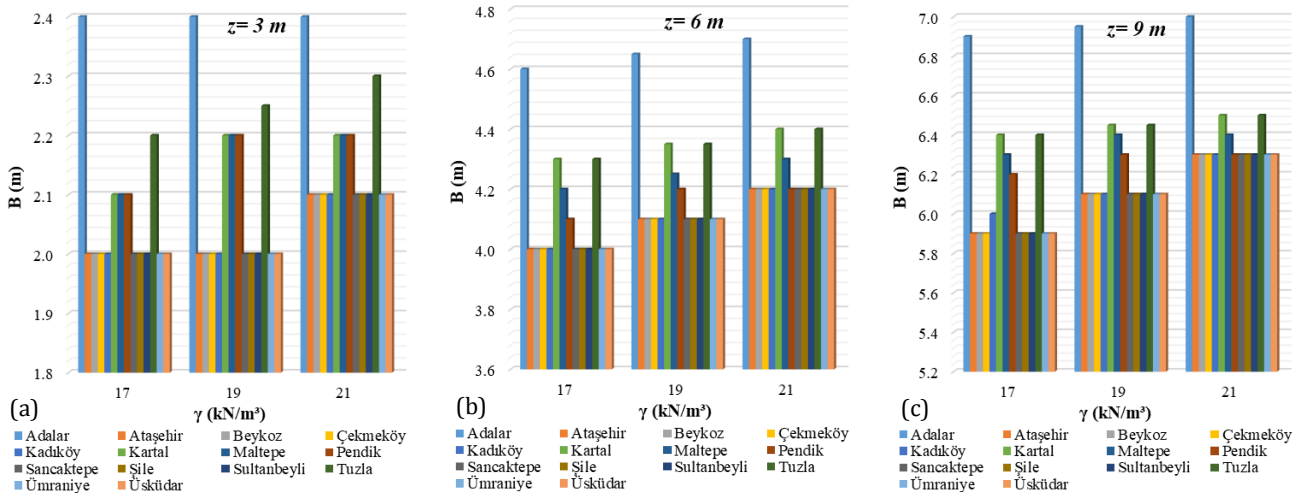

Fig. 7. The change of *B* against the unit weight of surrounding soil: (a) *z*=3 m; (b) *z*=6 m; (c) *z*=9 m.

In Fig. 7c, for *z*=9 m situation, the largest foundation bases were determined for Adalar district and 6.90, 6.95, 7.00 m lengths were obtained for the change of soil unit weight to 17 kN/m^3, 19 kN/m^3, 21 kN/m^3 respectively. In addition, the value of *B* during the change of soil unit weight to 17 kN/m^3, 19 kN/m^3, 21 kN/m^3 respectively, were determined for Kartal and Tuzla districts were 6.40, 6.45, 6.50 m; for Maltepe district 6.30, 6.40, 6.40 m; for Pendik district 6.20, 6.30, 6.30 m; for Kadıköy district 6.00, 6.10, 6.30 m and for all of the other districts 5.90, 6.10 and 6.30 m. As a result of the change in soil unit weight, the biggest rate of design change is determined at *z*=9 m situation which is accessing to 7%. The mentioned dimensions calculated for different districts under the effect of the soil unit weight change remarks that the increase of the excavation depth brings out the considerable influence of the soil unit weight. Furthermore, it is a noticeable result that the effect of the increase of S_{DS} value has an inversely proportional rate with the increase of soil unit weight values. This means that the remarkable change of the *B* width can be obtained for the districts that have relatively smaller S_{DS} values.

In Fig. 8, the effect of the surcharge loading is investigated according to the change of location and depending on the differentiation of *B*/*H* ratio. Accordingly, the effects of the absence of the surcharge loading and the increase of the loading magnitude to 15 kPa was both investigated. Within the context of the analyses conducted in this part of the study, the unit weight (19 kN/m^3) and the shear strength angle (32°) of the surrounding soil was assumed to be constant. The ratio of *B*/*H* has an importance in terms of design practice because traditionally, the beginning step of the design process of the retaining walls consists of the selection of some of the sizes in relation with the empirical approaches (Azizi 2000; Bowles 1979). This process can be named as proportioning and allows the designer to apply an iterative process to take place whereby the dimensions are adjusted at the end of the calculations. In this context, depending on the traditional proportioning process in the literature the width of the foundation base is suggested to be between 0.5-0.7 times the total length of the wall. Considering this situation in Fig. 8, the *B*/*H* ratios were planned to be compared to each other depending on the change of location and the surcharge loading condition. The increase of the surcharge loading amount, has increased the determined ratios of *B*/*H* as expected. The wall designs that were obtained in Adalar district for both *q*=0 and *q*=15 kPa situations give *B*/*H* ratios bigger than 0.7 value which is suggested to be the upper limit for the proportioning of the base width of the wall. The other districts exhibit similar rates with each other in terms of *B*/*H* ratio and the designs are almost remained between the envisaged proportioning limits in the literature. Besides, the consideration of relatively smaller excavation depths leads the design to be enlarged depending on the increase of the surcharge magnitude.

This means that if the excavation depth is 3 m, the width of the base can exceed the foreseen dimensions when the surcharge amount is raised. In addition to all these, the biggest change in the *B/H* ratio depending on the increase of the surcharge amount is obtained for *z*=3 m for all districts except Adalar and Tuzla. From a different viewpoint, the effects of the increase of the surcharge magnitude on the wall design process was also investigated in terms of the base width change in Fig. 9.

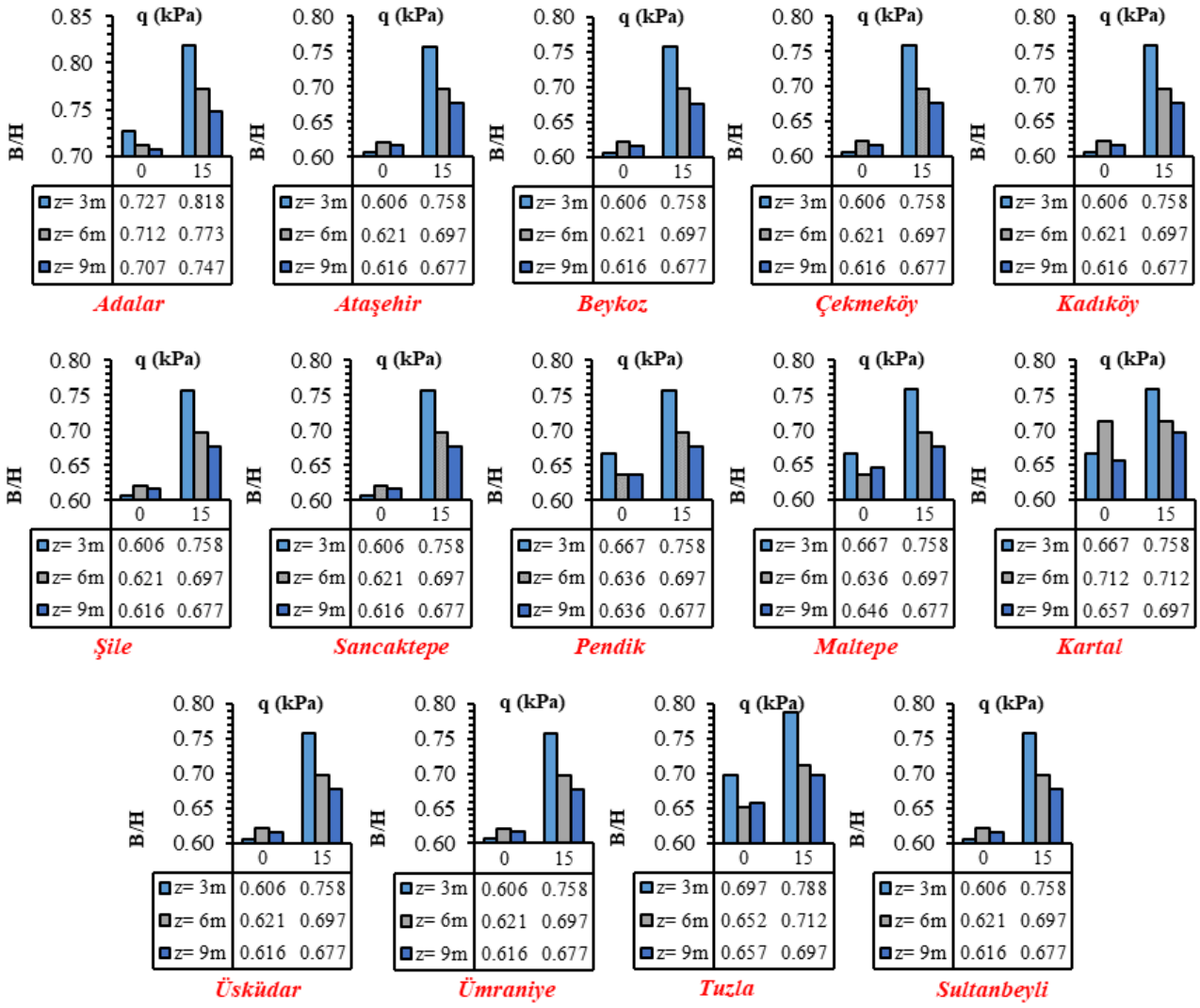

Fig. 8. The change of *B*/*H* ratio against the surcharge loading depending on the districts.

In addition, hand calculations have been also performed to reflect the location effect that is newly considered within the application details of TBEC-2018. The hand calculations were performed depending on the simplified pseudo-static approach of Mononobe-Okabe theory (Okabe 1924; Mononobe and Matsuo 1929). All the analyses were conducted with the use of constant values for the unit weight (19 kN/m^3) and the shear strength angle (32°) of the surrounding soil. The pseudo-static analyses for *q*=0 situation resulted with the determination of the necessitated average *B* values for 3 m, 6 m and 9 m excavation depths as 2.1 m, 4.6 m and 6.5 m respectively. The increase of the surcharge loading magnitude to 15 kPa increases the average *B* width to 3.2 m, 5.4 m and 7.0 m for 3 m, 6 m, 9 m excavation depths respectively. From Fig. 9, the evaluation of the analyses results show that the upper and lower amounts of the *B* widths were determined 2.4 m and 2.0 m (for *q*=0, *z*=3 m), 2.7 m and 2.5 m (for *q*=15 kPa, *z*=3 m), 4.7 m and 4.1 m (for *q*=0 kPa, *z*=6 m), 5.1 m and 4.6 m (for *q*=15 kPa, *z*=6 m), 7.0 m and 6.1 m (for *q*=0 kPa, *z*=9 m), 7.4 m and 6.7 m (for *q*=15 kPa, *z*=9 m) respectively.

The comparison of the pseudo-static approach and the application of TBEC-2018 shows that the pseudo-static approach gives reasonable average values for B which are remaining between the upper and lower limits determined by the use of TBEC-2018 for the absence of surcharge loading condition. On the other hand, the increase of the surcharge loading magnitude leads the pseudo-static approach solutions to be unacceptable in comparison with the solutions of TBEC-2018. This result demonstrates that depending on the crucial hazard of earthquakes in Turkey especially Istanbul, the usage of the location effect has an important necessity to ensure safety.

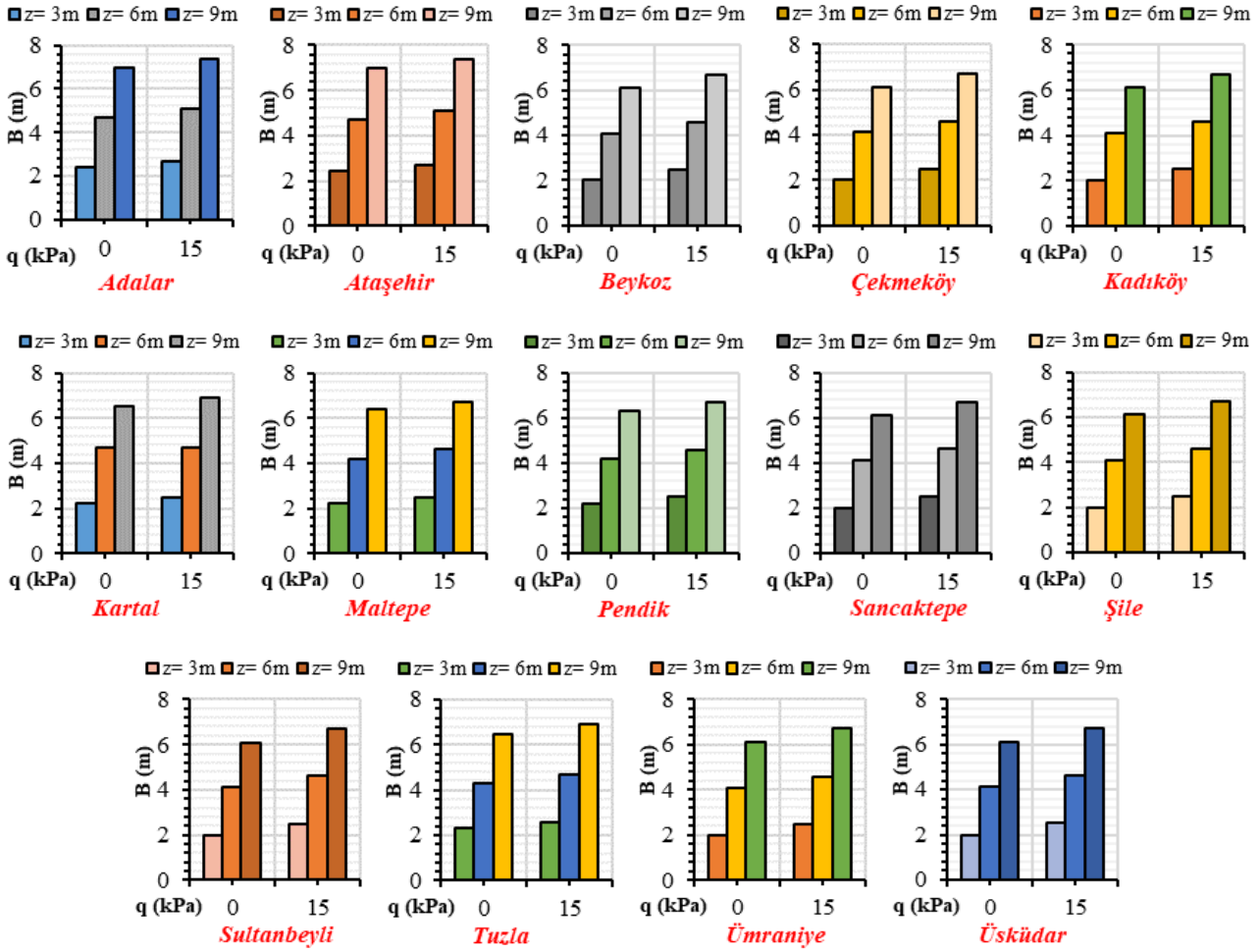

Fig. 9. The change of the *B* against the surcharge loading depending on the districts.

5. Conclusions

This study is prepared depending on the new design methodology suggested by TBEC-2018 for the design of reinforced concrete RWs under the action of both static and seismic loading conditions. A set of analyses have been planned according to the change of peak ground acceleration values which were obtained depending on the coordinates of the project site from the Earthquake hazard map of Turkey. The coordinates of the project sites were arranged for the districts of Istanbul Province Anatolian side to control the differentiation rate of the dimensioning of the wall system in terms of the foundation base width. In this context, based upon the assumption of same soil class usage, 14 different districts were selected and also the effects of the supported earth fill depth, the unit weight and shear strength angle values of surrounding soil strata, the surcharge load magnitude on the design of retaining walls have been investigated. In total 1260 design analyses were conducted within the scope of the location effect evaluation on the dynamic response of RWs. A comparative interpretation process was applied to the outcomes of the analyses and the following conclusions were obtained:

- The increase of the excavation depth leads the design to enlarge the base of the wall foundation.
- The wall designs are not affected by the change of the coordinate of the project site if relatively smaller depths (smaller than 6 m) are excavated within the soils which has smaller shear strength angle values. This may be because of the attainment of the limit design sizing due to the smallness of the soil strength.
- The increase of the shear strength angle ensures the surrounding soil to support the additional loads such as the earthquake loads. Therefore, it is expected to reduce the sizing of retaining wall if the increase of the shear strength angle of the surrounding soil medium is possible.
- For all the foreseen excavation depths studied in the context of this study, the maximum dimensions were obtained for the case that minimum shear characteristics were used. In addition, the width of the foundation value possesses the biggest amount for the biggest value of S_{DS} that is increasing the affected active total earth pressure value. This trend shows that the foundation width is directly proportional with the change of S_{DS} value. This situation remarks that it is not possible to use a standard type section proposed in the projecting of retaining walls.
- For relatively smaller excavation depths, the increase of soil unit weight has no effect on the width of the foundation base. However, for deeper excavations,

there happens an increase for the width of the foundation base approximately at the degree of 5% between the loosest and densest states of the surrounding soil strata.

- The deepen the excavation depth or the increase of the supported earth fill thickness has an integrated effect with the change of soil unit weight on dimensioning of the wall. The acquired widths for B determination shows the increase rate of the effect of soil unit weight rises with the decrease of S_{DS} value.
- It is a noticeable result that the effect of the increase of S_{DS} value has an inversely proportional rate with the increase of soil unit weight values. This means that the remarkable change of the B width can be obtained for the districts that have relatively smaller S_{DS} values.
- The increase of the surcharge loading amount, has increased the determined ratios of B/H as expected.
- The consideration of relatively smaller excavation depths leads the design to be enlarged depending on the increase of the surcharge magnitude. In addition to all these, the biggest change in the B/H ratio depending on the increase of the surcharge amount is obtained for the shallow depth for all districts except Adalar and Tuzla.
- The comparison of the pseudo-static approach and the application of TBEC-2018 shows that the pseudo-static approach gives reasonable average values for B width which are remaining between the upper and lower limits determined by the use of TBEC-2018 for the absence of surcharge loading condition.
- On the other hand, the increase of the surcharge loading magnitude leads the pseudo-static approach solutions to be unacceptable in comparison with the solutions of TBEC-2018.

All of these outcomes demonstrates that depending on the crucial risk of earthquake hazard of Turkey, the usage of the location effect has an important necessity to ensure safety. Consequently, the consideration of the location effect throughout the design process of reinforced concrete retaining walls has remarkable influence in terms of dimensioning and also cost.

Acknowledgements

None declared.

Funding

The authors received no financial support for the research, authorship, and/or publication of this manuscript.

Conflict of Interest

The authors declared no potential conflicts of interest with respect to the research, authorship, and/or publication of this manuscript.

References

AFAD (2021). Deprem Katoloğu. T.C. İçişleri Bakanlığı Afet ve Acil Durum Yönetimi Başkanlığı, Deprem Dairesi Başkanlığı, https://deprem.afad.gov.tr/depremkatalogu; https://deprem.afad.gov.tr/ddakatalogu. Downloaded on 03-02-2021. (in Turkish)

Ahmadi-Nedushan B, Varaee H (2009). Optimal design of reinforced concrete retaining walls using a swarm intelligence technique. *Proceedings of the 1st International Soft Computing Technology in Civil, Structural and Environmental Engineering*, Stirlingshire, Scotland, 1-12.

Akkar S, Azak TE, Can T, Çeken U, Demircioğlu MB, Duman TY, Erdik M, Ergintav S, Kadirioglu FT, Kalafat D, Kale Ö, Kartal RF, Kekovalı K, Kılıç T, Özalp S, Poyraz SA, Sesetyan K, Tekin S, Yakut A, Yılmaz MT, Yücemen MS, Fercan Ö (2018). Evaluation of seismic hazard maps in Turkey. *Bulletin of Earthquake Engineering*, 16(8), 3197-3228.

Aksoylu C, Mobark A, Arslan MH, Erkan İH (2020). A comparative study on ASCE 7-16, TBEC 2018 and TEC-2007 for reinforced concrete buildings. *Revista de la Construcción*, 19(2), 282-305.

Atmaca N, Atmaca A (2019). Comparison of 2018 and 2007 Turkish Earthquake Regulations. *The International Journal of Energy & Engineering Sciences*, 4(2), 19-25.

Azizi F (1999). Applied Analyses in Geotechnics. Taylor and Francis Group, New York.

Bowles JE (1988). Foundation Analysis and Design. McGraw-Hill, New York.

Dagdeviren U, Kaymak B (2020). A regression-based approach for estimating preliminary dimensioning of reinforced concrete cantilever retaining walls. *Structural and Multidisciplinary Optimization*, 61, 1657-1675.

Elçi H, Göker KA (2018). Comparison of earthquake codes (TEC 2007 and TBEC 2018) in terms of seismic performance of RC columns. *International Journal of Scientific and Technological Research*, 4(6), 9-21.

Gürsoy Ş (2013). İstinat duvarlarına etkiyen aktif zemin etkilerinin Eurocode-8 ve Türkiye Deprem Yönetmeliğine göre karşılaştırılması. *Gazi University Journal of Science Part C: Design and Technology*, 1(4), 153-160.

Kaveh A, Khayatazad M (2014). Optimal design of cantilever retaining walls using ray optimization method. *Iranian Journal of Science and Technology, Transactions of Civil Engineering*, 38(C1), 261-274.

Kayhan AH, Demir A (2018). Statik ve dinamik yüklere maruz betonarme konsol istinat duvarlarının diferansiyel gelişim algoritması ile optimum tasarımı. *Pamukkale University Journal of Engineering Sciences*, 24(3), 403-412. (in Turkish)

Keskin E, Bozdoğan KB (2018). 2007 ve 2018 Deprem Yönetmeliklerinin Kırklareli İli özelinde değerlendirilmesi. *Kırklareli University Journal of Engineering and Science*, 4-1, 74-90. (in Turkish)

Konstandakopoulou F, Tsimirika M, Pnevmatikos N, Hatzigeorgiou GD (2020). Optimization of reinforced concrete retaining walls designed according to European Provision. *Infrastructures*, 5(6), 46-62.

Kramer SL (1996). Geotechnical Earthquake Engineering. Prentice-Hall, USA.

Özberk L, Kahyaoğlu MR (2018). Dayanma yapılarının DBYBHY ve TBDY göre analiz sonuçlarının karşılaştırılması ve tespitler. *Proceedings of the Soil Mechanics and Geotechnical Engineering 17th National Conference*, İstanbul, Turkey. (in Turkish)

Öztürk M (2018). 2018 Türkiye Bina Deprem Yönetmeliği ve Türkiye Deprem Tehlike Haritası ile ilgili İç Anadolu Bölgesi bazında bir değerlendirme. *Journal of Selcuk-Technic*, 17(2), 31-42. (in Turkish)

TBEC-2018 (2018). Türkiye Bina Deprem Yönetmeliği, T.C. İçişleri Bakanlığı Afet ve Acil Durum Yönetimi Başkanlığı, Ankara, Turkey. (in Turkish).

TDTH (2018). Türkiye Deprem Tehlike Haritaları İnteraktif Web Uygulaması. T.C. İçişleri Bakanlığı Afet ve Acil Durum Yönetimi Başkanlığı, https://deprem.afad.gov.tr/deprem-tehlike-haritasi. Downloaded on 03-02-2021. (in Turkish)

Uray E, Çarbaş S, Erkan İH, Tan Ö (2019). Parametric investigation for discrete optimal design of a cantilever retaining wall. *Challenge Journal of Structural Mechanics*, 5(3), 108-120.

Yüksel YZ, Akbaş ŞD (2020). İstinat duvarlarına etki eden statik ve dinamik toprak basınç kuvvetlerinin TDY-2007 ve TBDY-2018 yönetmeliklerine göre karşılaştırılması. *Proceedings of the 4th International Symposium on Natural Hazards and Disaster Management*, Bursa, Turkey, 834-840. (in Turkish)